RESEARCH ARTICLE | SEPTEMBER 19 2025

Modeling symmetric and asymmetric hysteresis modes in patterned microchannels: A unified framework for classification and prediction *⊗*

Heng-yu Hu (胡恒瑜) ⑩ ; Hai-bo Huang (黄海波) ■ ⑩



Physics of Fluids 37, 093364 (2025) https://doi.org/10.1063/5.0288009





Articles You May Be Interested In

Investigation of oil/water two-phase flow behavior in laminated shale porous media considering heterogeneous structure and fluid-solid interaction

Physics of Fluids (March 2024)

Simulation of multicomponent multiphase flow using lattice Boltzmann method

AIP Conf. Proc. (June 2012)

Study on the evolution and stability of gas-liquid interfaces based on composite structures on the sidewall surface of a microchannel

Physics of Fluids (August 2023)



Physics of Fluids

Special Topics Open for Submissions

Learn More



Modeling symmetric and asymmetric hysteresis modes in patterned microchannels: A unified framework for classification and prediction

Cite as: Phys. Fluids **37**, 093364 (2025); doi: 10.1063/5.0288009 Submitted: 28 June 2025 · Accepted: 3 September 2025 · Published Online: 19 September 2025







Heng-yu Hu (胡恒瑜) 🕞 and Hai-bo Huang (黄海波) 🗈 🕞



AFFILIATIONS

Department of Modern Mechanics, University of Science and Technology of China, Hefei, Anhui Province 230027, China

a) Author to whom correspondence should be addressed: huanghb@ustc.edu.cn

ABSTRACT

This study explores contact angle hysteresis (CAH) in non-uniform patterned microchannels through lattice Boltzmann method simulations. A novel hybrid-effect-dominated-hysteresis (HDH) mode, integrating individual-effect-dominated hysteresis (IDH) and collective-effectdominated hysteresis (CDH), is identified, caused uniquely from non-uniform heterogeneity. The contact line jumping process is modeled as a mass-spring-damper system, offering a clear force-balance framework for explaining and predicting CAH. A graphical force-balance approach proposes the Ec-Cc criterion and constructs a phase diagram framework that classifies CAH modes into IDH, CDH, and HDH. This framework provides a unified methodology for analyzing CAH across two-dimensional and three-dimensional microchannel geometries, enabling accurate predictions for diverse designs. This work provides key insight into contact line dynamics and practical tools for controlling the motion of the contact line in heterogeneous systems.

Published under an exclusive license by AIP Publishing. https://doi.org/10.1063/5.0288009

I. INTRODUCTION

Wetting and spreading phenomena play a vital role across a diverse range of fields, including industrial processes, agricultural applications,² and engineering practices.³ When another fluid displaces one, the motion of the contact line (MCL) occurs, which is intricately influenced by physicochemical interactions between the fluid and the solid surface. If the surface has physical roughness or chemical heterogeneity, contact angle hysteresis (CAH) and associated complex MCL will result.⁵ In other words, modifying the chemical heterogeneity of the surface can tailor specific wetting properties and MCL.⁶ In the previous study, advancements in surface engineering have introduced innovative methods to achieve precise control over wetting behavior, notably through developing patterned surfaces that exhibit inherent heterogeneity. For instance, Jung and Bhushan fabricated micro- and nanopatterned surfaces that mimic natural roughness-induced hydrophobicity. The MCL on physical roughness or chemical heterogeneity surfaces has attracted substantial interest within academic and industrial communities because it contributes to achieving precise control over fluid on solid surfaces.

Significant research has been dedicated to understanding the MCL on physical roughness or chemical heterogeneity surfaces in two-dimensional (2D) systems where the contact line is straight or

maintains constant curvature due to axisymmetry. Examples include chemically striped surfaces, 9,10 sinusoidal surfaces, 11-15 and surfaces featuring posts, 16,17 investigated through analytical and numerical methods. After the extension of this analysis to three-dimensional (3D) systems, researchers have explored striped patterns, ¹⁸ regular lattices of posts, 19-21 and chemical patches. 22 The physical roughness and chemical heterogeneity of patterned surfaces introduce complex often characterized by slip-stick^{25,26} and slip-jump motions.²⁷ Stick-slip behavior occurs when the contact line becomes pinned near strong surface defects, 15 with the magnitude and position of the contact line jumps being highly sensitive to the surface patterning. These dynamics can vary significantly in different directions of the patterned surfaces, further underscoring the intricate interplay between surface structure and wetting behavior.²

In addition to the complex MCL, contact angle hysteresis (CAH), as a common phenomenon in wetting processes, is defined by the discontinuity between the receding and advancing contact angles.^{28,29} It is widely acknowledged that substrate heterogeneity, including chemical heterogeneity, is the primary cause of CAH. 12,29,30 This conclusion makes CAH a critical factor in optimizing and controlling wetting processes.³¹ For instance, CAH in microchannels can highlight wettability effects on pore-filling events.³² Various methods have been developed

to research CAH, including capillary rise techniques, 33-35 moving tape methods, 36-38 and direct measurement and control of CAH in electrified ionic liquids, which guides future experimental validation.³⁹ In these research works, sessile droplet system are widely used, where a drop is quasi-statically inflated or deflated using, for example, a micropipette. 40-46 Here, the deformation of the gas-liquid interface (GLI) depends not only on the solid surface properties but also on the droplet volume, 47 often resulting in irregular oscillatory curves that complicate the statistical analysis of CAH. 12 To address these challenges, researchers have applied chemically heterogeneous channels to study CAH. 15,31,47,48 These studies used the scaling law based on the mechanical balance between capillary forces exerted by surface defects and the elastic restoring forces acting on the contact line, which was proposed by Joanny and De Gennes.³⁰ For instance, Chang et al.⁴⁷ extended it to account for two new distinct types: individual-effectdominated hysteresis (IDH) and collective-effect-dominated hysteresis (CDH). Despite these advancements, researchers like Chang et al. did not give a strict mathematical proof that Joanny and de Gennes' model applies to CAH in heterogeneous microchannels with equal-width patterns nor did they explore CAH modes or scaling laws in the nonequal-width or non-uniform situations, which are more general. As a result, this area of research remains underexplored, and there is a critical need for a comprehensive model that accounts for the influence of heterogeneity parameters on CAH.

This study addresses the above-mentioned unresolved issues by integrating numerical simulations and theoretical modeling to investigate the complex MCL and CAH in heterogeneous microchannels. We derived the prerequisite conditions for contact line jumps using force balance principles and classical mechanical models. In addition, we identified a new CAH mode distinct from the previously defined IDH and CDH. To differentiate these three modes effectively, we developed the criteria that map the modes onto the four quadrants of a phase diagram. Furthermore, a formula was proposed to quantitatively describe the relationship between microchannel heterogeneity parameters and CAH, offering greater accuracy and predictive capability. The conclusion is mainly based on the 2D system, and then we expand it to make the conclusion applicable to the 3D system.

The remainder of this paper is organized as follows. The problem statement and mathematical formulation are presented in Sec. II. The research methodology is described in Sec. III. Detailed results for 2D and 3D cases are discussed in Secs. IV and V, respectively. Finally, conclusions are presented in Sec. VI.

II. PROBLEM STATEMENT

A. Physical problem

All the physical problems examined in this study are based on the evaporation and condensation occurring within patterned heterogeneous microchannels, which are symmetrical along the dashed line from left to right (Fig. 1). The microchannel has a width b, with rigid, flat, and smooth surfaces. The inner surfaces of the channel exhibit chemical patterned heterogeneity achieved by the alternating arrangement of defects and background. The defects on the upper and lower boundaries are identical. The spatial feature length of surface heterogeneity is denoted as β . In other words, up to one complete defect can be contained within β . The width of defects within each feature length is determined by λ_n , and n is a positive integer. In the 3D case, the defects are modeled as rectangular regions with λ_n and λ_y in the x- and y-

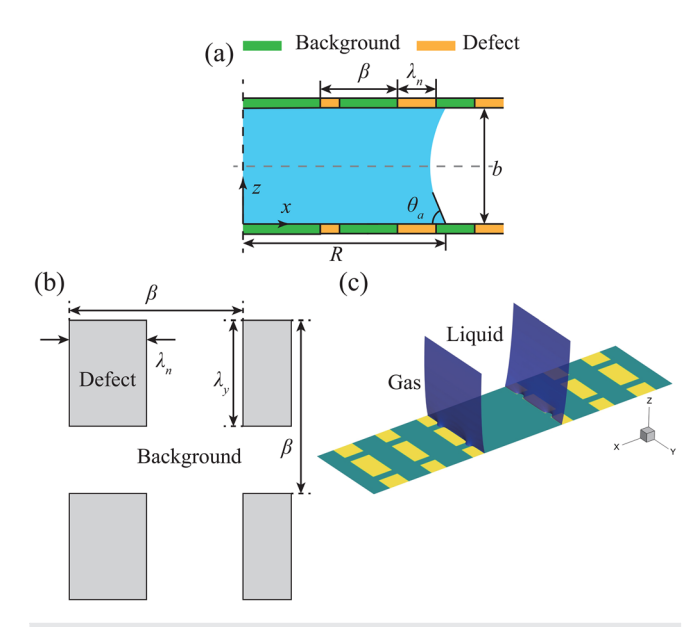


FIG. 1. Schematic diagrams of a droplet in a microchannel with a chemically heterogeneous substrate. (a) Diagram illustrating the non-uniform two-dimensional (2D) case. The black and gray dotted lines, respectively, represent the left-right and up-down symmetries of the domain. (b) Representation of substrate defects in three-dimensional (3D) non-uniform situations. (c) Depiction of a droplet interacting with the substrate in 3D (the lower part).

directions, respectively. The range of λ_n is constrained to $0 \le \lambda_n \le 0.5 \beta$, and we suppose the width of defects in the y-direction is constant with space. When $\lambda_y = \beta$, the 3D case simplifies to a 2D scenario. For $\lambda_n = \text{const} = 0.5 \beta$, the defect width in the x-direction equals that of the background, corresponding to equal-width patterned heterogeneity. Conversely, for $\lambda_n = \text{const}$ and $0 \le \lambda_n < 0.5 \beta$, the width difference between the defect and the background is disrupted, leading to the non-equal-width situation. More generally, when $\lambda_n \ne \text{const}$ and $0 \le \lambda_n < 0.5 \beta$ are satisfied, it is defined as a non-uniform situation that characterizes the complex patterned heterogeneity. The non-uniform situation is the focus of our research.

As illustrated in Fig. 2(a), the wettability of defects and the background is defined by the intrinsic contact angle θ_i . The relationship between the solid–liquid, solid–gas, and liquid–gas surface tensions (γ_{sl} , γ_{sg} , and γ) is governed by the Young equation as follows:

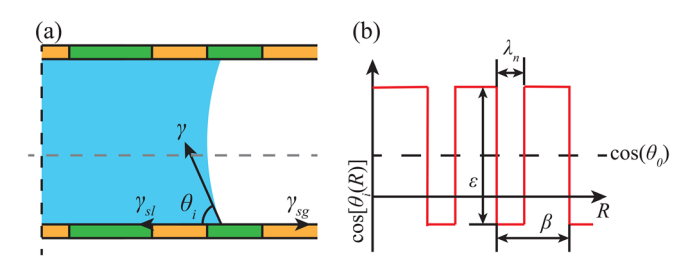


FIG. 2. Schematic diagram of (a) the intrinsic contact angle defined by the Young equation and (b) mesa defects.

$$\cos \theta_i = \frac{\gamma_{sg} - \gamma_{sl}}{\gamma}.\tag{1}$$

The wettability is characterized by a position-dependent variation in the solid-liquid tensions γ_{sl} and solid-gas tensions γ_{sg} , while interfacial tensions y remain constant. The defects are modeled as sharpedged structures (mesa), where the change in wettability from the background to the defects occurs discontinuously. Consequently, the wettability of the background and the stripes are given by $\cos(\theta_0)$ $+\varepsilon/2$ and $\cos(\theta_0) - \varepsilon/2$, respectively, as shown in Fig. 2(b). Here, ε and θ_0 represent the strength of the heterogeneity and the reference contact angle, respectively. The droplet is initially positioned at the center of the microchannel to maintain symmetry (both left-right and top-bottom). In the 2D cases, the base radius R is defined as the distance from the contact line to the center. The maximum value of *R* is half the microchannel length, denoted R_b . Suppose there are a total of N defects in the microchannel, then add an extra area of length 2β , and the $R_b = (N+2)\beta$. The apparent contact angle of the droplet is defined as θ_a . The volume of droplets is controlled through evaporation and condensation. During evaporation, the contact line recedes with the diminishing volume, and it advances during condensation.

B. Mathematical formulation

After defining the physical problem and establishing the coordinate system, we make several reasonable assumptions to describe the droplet's state quantitatively. At the initial moment, the system is assumed to be in a state of stationarity. During the simulation, no external volume forces, including gravity, keep the system isothermal. The MCL is driven solely by density differences and is relatively slow, so the system remains in a quasi-steady state, except during droplet jumps. In the 2-D cases, the GLI is approximated as a standard meniscus, allowing the droplet volume to be expressed as follows:

$$V(R) = 2Rb + 2b^2 \left[\frac{2\theta_a - \pi + \sin(2\theta_a)}{8\cos^2\theta_a} \right]. \tag{2}$$

The free energy E analysis can demonstrate the system's stability. For a fixed droplet volume, the free energy, per unit length of the contact line and up to a constant, can be calculated by³¹

$$E(R) = \gamma b \left(\frac{\pi - 2\theta_a}{\cos \theta_a} \right) - 4\gamma \int_0^R \cos \left[\theta_i(r) \right] dr.$$
 (3)

Minimize the free energy with a fixed droplet volume V to obtain the equilibrium configurations: the apparent contact angle θ_a equals the inherent contact angle θ_i defined by the Young equation, i.e.,

$$\cos[\theta_a(R)] = \cos[\theta_i(R)]. \tag{4}$$

We introduce the diffuse interface model, which considers the GLI to have a certain thickness, defined as the interfacial thickness ξ . In this model, for surfaces containing chemical heterogeneity defects, the local Cassie–Baxter (LCB) equation needs to be introduced to perform more accurate calculations of the apparent contact angle when the interface is located at the junction of the background and defect. The LCB equation is as follows:

$$\cos \theta_a = \frac{1}{\xi} [l_A \cos \theta_{Ai} + l_B \cos \theta_{Bi}], \tag{5}$$

where θ_{Ai} and θ_{Bi} are the intrinsic contact angles of background and defects, respectively. l_A and l_B are the thicknesses of the diffused interface occupied by background and defects, respectively. l_A and l_B satisfy $l_A + l_B = \xi$. Equation (5) equivalent to Eq. (4) when the contact line is far from the intersection of defects ($l_A = \xi$ or $l_B = \xi$).

This paper defines the following dimensionless variables: Reynolds number $Re=U_c\beta/\nu^\sigma$, Peclet number $Pe=U_c\beta/D$, Capillary number $Ca=\rho^\sigma\nu^\sigma U_c/\gamma$, and Cahn number $Cn=\xi/\beta$. Here, U_c and ξ are characteristic velocity and interfacial thickness, respectively. In this study, the spatial feature length of surface heterogeneity β and other parameters are chosen as characteristic quantities to normalize the physical quantities as follows:

$$b^* = \frac{b}{\beta},\tag{6a}$$

$$R^* = \frac{R}{\beta},\tag{6b}$$

$$V^* = \frac{V}{\beta^2},\tag{6c}$$

$$E^* = \frac{E}{\beta \gamma}.$$
 (6d)

It is noted that $V^* = V/\beta^3$ for 3D cases. For simplicity, we will drop the asterisk notation in the remainder of the paper.

III. RESEARCH METHOD

The multicomponent multiphase pseudopotential lattice Boltzmann method (MCMP-LBM), proposed by Shan and Chen, ⁵⁰ is applied to simulate in 2D and 3D in this paper. This method has been validated through complex multiphase flow modeling. ⁵¹ It simulates the fluid by calculating the distribution functions of each component $f_i^{\sigma}(\mathbf{x},t)$ (distinguished using superscript σ and $\bar{\sigma}$). All component distribution functions follow the following evolution equation:

$$f_i^{\sigma}(\mathbf{x} + \mathbf{e}_i \Delta t, t + \Delta t) = f_i^{\sigma}(\mathbf{x}, t) - \frac{\Delta t}{\tau^{\sigma}} \left[f_i^{\sigma}(\mathbf{x}, t) - f_i^{\sigma, eq}(\mathbf{x}, t) \right], \quad (7)$$

where \mathbf{e}_i (i = 0, 1, ..., 8 for 2D cases and i = 0, 1, ..., 18 for 3D cases) are the discrete velocities. The relaxation time τ^{σ} is a parameter related to the kinematic viscosity of the fluid. Δx and Δt are grid spacing and time step. In MCMP-LBM, an equilibrium distribution function $f_i^{\sigma,eq}$ is calculated by

$$f_i^{\sigma,eq}(\mathbf{x},t) = \omega_i \rho^{\sigma} \left[1 + \frac{\mathbf{e}_i \cdot \mathbf{u}^{\sigma}}{c_s^2} + \frac{(\mathbf{e}_i \cdot \mathbf{u}^{\sigma})^2}{2c_s^4} - \frac{(\mathbf{u}^{\sigma})^2}{2c_s^2} \right].$$
(8)

The density ρ^σ and macroscopic velocity \mathbf{u}^σ of each component fluid are

$$\rho^{\sigma} = \sum_{i} f_{i}^{\sigma},\tag{9}$$

$$\mathbf{u}^{\sigma} = \mathbf{v} + \frac{\tau^{\sigma} \mathbf{F}^{\sigma}}{\rho^{\sigma}}.\tag{10}$$

Here, ${\bf F}^{\sigma}$ is the volume force acting on each component fluid and ${\bf v}$ is the overall velocity of the fluid system, which is defined as 50

$$\mathbf{v} = \frac{\sum_{\sigma} \sum_{i} \frac{f_{i}^{\sigma} \mathbf{e}_{i}}{\tau^{\sigma}}}{\sum_{\sigma} \frac{\rho^{\sigma}}{\tau^{\sigma}}}.$$
 (11)

The mixture density ρ , velocity **u**, force \mathbf{F}^{σ} , and interparticle potential $\psi^{\sigma}(\mathbf{x},t)$ are respectively calculated by

$$\rho = \sum_{\sigma} \rho^{\sigma},\tag{12}$$

$$\rho = \sum_{\sigma} \rho^{\sigma}, \qquad (12)$$

$$\mathbf{F}^{\sigma}(\mathbf{x}, t) = -G\psi^{\sigma}(\mathbf{x}, t) \sum_{i} \omega_{i} \psi^{\bar{\sigma}}(\mathbf{x} + \mathbf{e}_{i} \Delta t, t) \mathbf{e}_{i}, \qquad (13)$$

$$\mathbf{u} = \frac{1}{\rho} \left(\sum_{\sigma} \sum_{i} f_{i}^{\sigma} \mathbf{e}_{i} + \frac{1}{2} \sum_{\sigma} \mathbf{F}^{\sigma} \Delta t \right), \tag{14}$$

$$\psi^{\sigma}(\mathbf{x},t) = \rho_0 \left[1 - e^{-\rho^{\sigma}(\mathbf{x},t)/\rho_0} \right]. \tag{15}$$

The lattice Boltzmann equation can reproduce the Navier-Stokes equations for fluid dynamics by applying the Chapman-Enskog expansion.56

The volume change of the droplet is driven by the density gradient with constant ambient pressure, which can be described by the unsteady diffusion equation (Fick's second law). Assuming that the density distribution is non-uniform mainly in the R direction and changes linearly according to the parameter δ , solving the ordinary differential equation gives 47

$$(V - V_0)(2bR_b - V - V_0) = -\frac{2b^2 - D\delta}{\rho^{maj}}.$$
 (16)

In this mechanism, the mass change rate of the droplet is dominated by the diffusion of the droplet into the surrounding environment, driven by the concentration or density gradient of the droplet's components in the surrounding fluid. The parameter δ plays a crucial role in determining both the direction and speed of the MCL. Specifically, when $\delta > 0$, the droplet undergoes evaporation and the contact line advances; when $\delta < 0$, it condenses and the contact line recedes. To accurately simulate these processes driven by density gradients, we employ the above MCMP-LBM-based model introduced by Hessling et al.,57 which has been validated against Fick's law. This model was also utilized by Chang et al.47 to simulate droplet evaporation and condensation within a microchannel. The density initialization scheme used in the model is detailed in Table I.

At the outlet boundary $(R = R_b)$, constant density and pressure are imposed, with the distribution function calculated using Eq. (8). Treating the upper (z = b) and lower (z = 0) boundaries requires careful consideration, as these boundaries must satisfy both no-slip and specific wetting conditions. The halfway bounce-back scheme, proposed by Ziegler,⁵⁸ enforces no-slip boundary conditions. This approach has been widely adopted in LBM simulations because it can

TABLE I. Density setting in MCMP-LBM according to Hessling et al.⁵⁷ and Chang et al.

	Gas	Liquid	
$ ho^{\sigma} ho^{ar{\sigma}}$	$ ho^{min} \ ho^{maj}$	$ ho^{maj} \ ho^{min}$	

accurately simulate no-slip conditions while ensuring strict mass conservation.⁵⁵ More basic introductions and validation for the wettability conditions are described in Appendix B.

The apparent contact angle θ_a is determined by directly measuring the gas-liquid interface (GLI). In this study, we define the curve (for 2D cases) or surface (for 3D cases) satisfying $\phi^{\sigma}(\mathbf{x}) = 0.5$ as the GLI, where the order parameter $\varphi^{\sigma}(\mathbf{x})$ is calculated based on the density as follows:

$$\varphi^{\sigma}(\mathbf{x}) = \frac{\rho^{\sigma}(\mathbf{x}) - \rho^{\min}}{\rho^{maj} - \rho^{\min}}.$$
 (17)

Table II presents the key physical parameters used in the simulations. For a specific flow problem, simulation parameters can be determined by specified dimensionless parameters according to Chang et al. 47 The mesh spacing in the x, y, and z directions is set to 1 lattice unit (lu), while the time step in the LBM simulations is set to 1 time step (ts). The grid resolution is controlled by the parameter β , which represents the number of lattice cells across a characteristic length, which is illustrated in Fig. 1. We have tested a series of resolutions in Appendix A, proving that $\beta = 50$ is suitable for our simulations.

IV. TWO-DIMENSIONAL RESULTS AND DISCUSSION

In this section, we first present the contact line behavior in typical cases. Since the jump plays a critical role, we then analyze the jump mode to identify when the jump occurs. During this analysis, we propose a model to explain and understand the criteria for jump initiation. Finally, we discuss CAH using the graphical construction of the force balance and propose criteria to distinguish between IDH, CDH, and HDH.

A. Overview of MCL

We conducted a series of non-uniform simulations by modifying parameters $(b, \varepsilon, \lambda_n, \text{ and } \theta_0)$. In these cases, λ_n varies linearly with space as follows:

TABLE II. Density setting in MCMP-LBM according to Hessling et al.⁵⁷ and Chang

Parameter/(unit)	Value
Re	0.003
Ca	0.000 025
Pe	0.0042
Cn	0.108
G	3.6
D	0.12^{57}
$eta/(\mathrm{lu})$	50
$R_b/(\mathrm{lu})$	500
$\rho^{maj}/(\mathrm{mu/lu}^3)$	0.7
$ ho^{\min}/(\mathrm{mu/lu^3})$	0.036
$ ho_0/(\mathrm{mu/lu}^3)$	1
$c_s/(lu/ts)$	$1/\sqrt{3}$

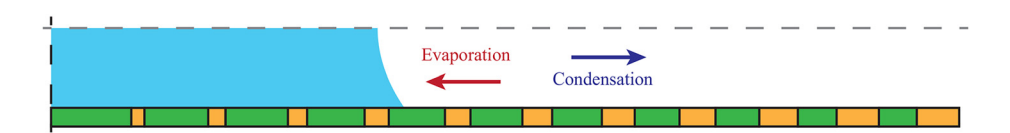


FIG. 3. The non-uniform heterogeneity generated from Eq. (18) with N = 10. Due to the symmetry of the structure, only the lower right part of the 2D computing domain is presented. The black and gray dotted lines respectively represent the left-right and up-down symmetries of the domain.

$$\lambda_n = \frac{0.35(n-1)}{N-1} + 0.15, \quad n = 1, 2, ..., N,$$
 (18)

which constructs the non-uniform heterogeneity in Fig. 3. Through base radius R, and apparent contact angle θ_a , we examined the MCL and the deformation of the GLI. The horizontal coordinates are V/b to eliminate the influence of different widths b on the length of curves.

Figure 4 presents the MCMP-LBM simulation results, with the arrangement of defects and background are shown in Fig. 3. They illustrating the relationships among the base radius R, and apparent contact angle θ_a as functions of V/b. The arrows indicate the temporal evolution of these variables. Evaporation and condensation indirectly drive the MCL by influencing the droplet volume. During condensation, the contact line advances (liquid displaces gas on the surface), while during evaporation, it recedes. The advancing and receding trajectories shown in Fig. 4 reveal distinct modes of MCL, including slip, stick, and jump modes. A specific set of points in Figs. 4(e) and 4(f) has been selected to illustrate these fundamental modes of MCL within the heterogeneous microchannel.

- Slip. Here, R change linearly with V, while θ_a remains constant.
 The contact line moves forward at a uniform rate. Examples of slipping during condensation are represented by I → II → III_C and IV → V, while slipping during evaporation corresponds to V → IV → III_E and II → I.
- Stick. At specific points, R remains nearly constant despite changes in V. During this phase, θ_a transitions gradually between the wettabilities of the background and defects, indicating that the contact line remains nearly stationary. Volume changes primarily manifest as deformation of the gas-liquid interface (GLI). The sticking behavior during condensation and evaporation is represented by V ↔ VI.
- Jump. During this mode, V remains almost unchanged (implying a very brief time interval). At the same time, R rapidly increases (during condensation) or decreases (during evaporation), and θ_a transitions abruptly between θ_i of the background and defects. The asymmetry of jump positions causes a divergence between the evaporation and condensation trajectories. Examples of condensation-related jumps include $III_C \rightarrow IV$, while evaporation-related jumps are represented by $III_E \rightarrow II$.

Figure 5 illustrate the MCL during evaporation and condensation for the cases of $\lambda_n=0.46$ (a, b) and $\lambda_n=0.27$ (c, d). The observed MCL is a combination of the above-mentioned fundamental modes. For $\lambda_n=0.46$ [corresponding to Figs. 4(e) and 4(f)], the MCL consistently cycles through the sequence of slip-jump-slip-stick, irrespective of whether condensation or evaporation occurs. This finding aligns with the results reported by Pradas *et al.*⁴⁴ and Chang *et al.*⁴⁷

However, our study reveals an additional detail: in certain cases, the MCL exhibits asymmetric behavior, where the modes differ between evaporation and condensation. For instance, as shown in Figs. 5(c) and 5(d) [corresponding to Figs. 4(c) and 4(d)], the MCL during condensation follows a slip-jump-slip-stick sequence, whereas, during evaporation, it follows a slip-jump-stick sequence. The asymmetry of the MCL during evaporation and condensation leads to an asymmetric CAH cycle, as shown in Fig. 6, which is a partial magnification of the hysteresis portion within one cycle in Figs. 4(d) and 4(f). This phenomenon, which has not been reported previously, represents a novel observation. Sections IV B and IV C explore the underlying mechanisms driving this phenomenon and its implications for CAH.

Figure 4 clearly illustrate the non-periodicity of θ_a in the non-uniform situation, a behavior different from earlier studies. ^{47,59,60} Inspired by Chang *et al.*, ⁴⁷ we define CAH as follows:

$$H \equiv \langle \cos \theta_R \rangle - \langle \cos \theta_A \rangle, \tag{19}$$

where θ_R and θ_A are the receding and advancing apparent contact angles, and the CAH in the defect located in $n < R \le n+1, n = 1, 2, ..., N$ can be calculated by

$$\langle \cos[\theta_A(V)] \rangle \equiv \frac{1}{\Delta V} \int_{\Delta V} \cos[\theta_A(V)] \, dV$$

$$= \frac{1}{2b} \int_{2bn}^{2b(n+1)} \cos[\theta_A(V)] \, dV, \qquad (20a)$$

$$\langle \cos[\theta_R(V)] \rangle \equiv \frac{1}{\Delta V} \int_{\Delta V} \cos[\theta_R(V)] \, dV$$

$$= \frac{1}{2b} \int_{2bn}^{2b(n+1)} \cos[\theta_R(V)] \, dV. \qquad (20b)$$

If the evaporation and condensation curves fully overlap throughout the entire process, no CAH is observed. However, due to heterogeneity, the contact line jump causes the curves to diverge. Consequently, the following analysis of the jump behavior is essential for understanding the mechanisms behind CAH.

B. The investigation of the jump mode

The contact line jump has been extensively studied as a physical phenomenon closely linked to CAH. MCL can be classified into two types: slip-jump-slip-stick and slip-jump-stick. To ensure the generality of the results, this paper does not distinguish between these two cases when analyzing the jump mode.

The Young equation [Eq. (1)] is reconstructed, and the dimensionless heterogeneity force f_h and elastic restoring force f_e are defined as

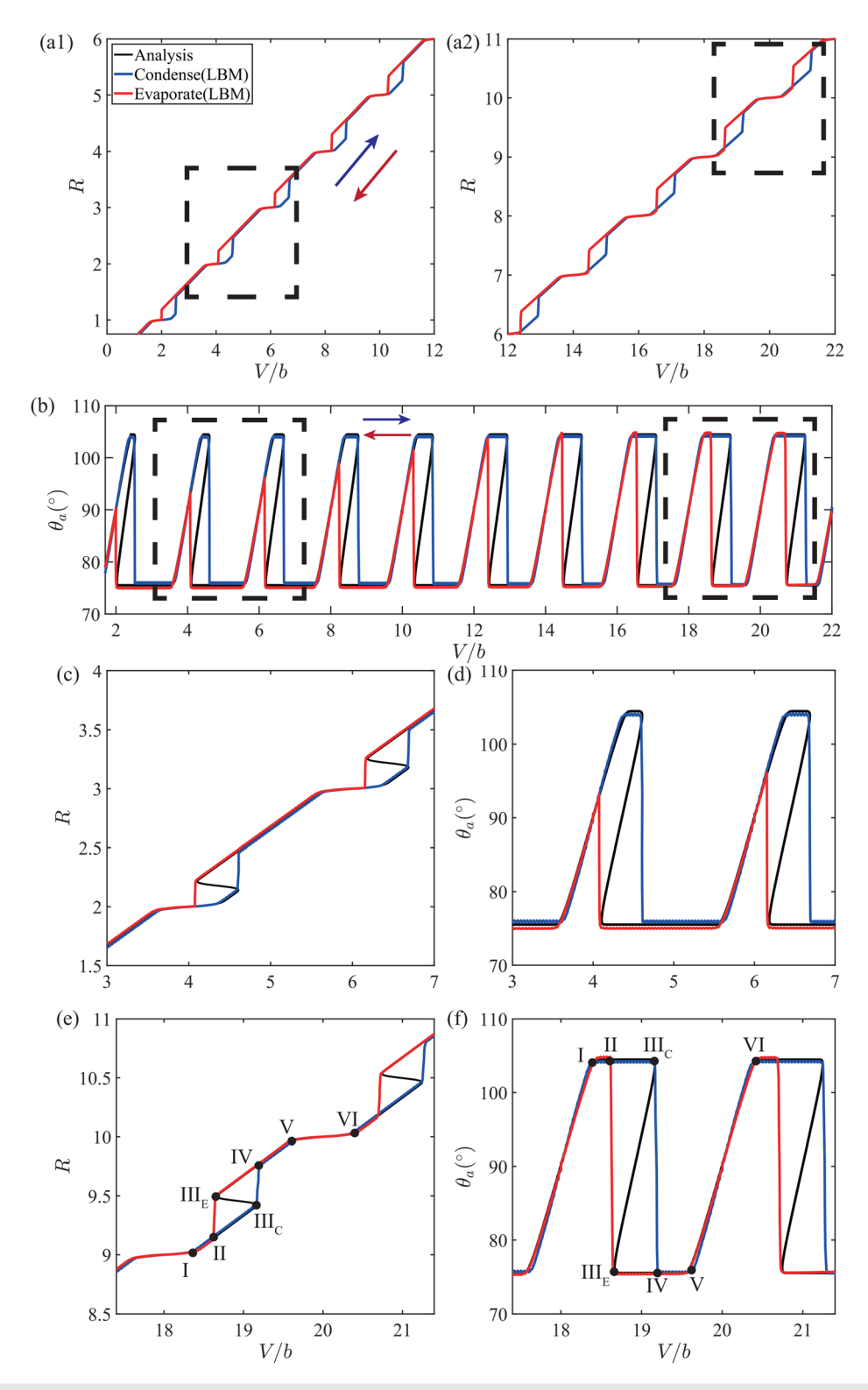


FIG. 4. The MCL simulated by MCMP-LBM and the comparison with the analytical method. The value of θ_0 , ϵ , N, and b are 90°, 0.5, 10, and 4.0, respectively. (a1), (a2), and (b) show the basic radius curves and contact angle curves. (c) and (d) and (e) and (f) are the zoomed-in views of (a) and (b) within the range of $V/b \in [3.0, 7.0]$ and $V/b \in [17.4, 21.4]$.

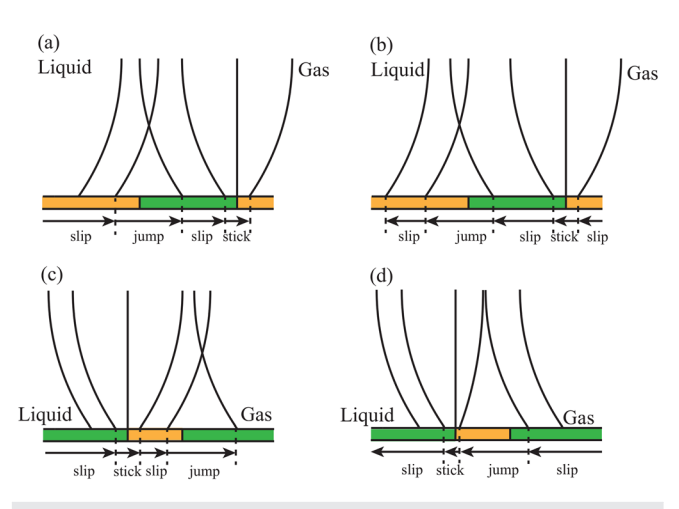


FIG. 5. Schematic diagrams illustrating MCL and the deformation and movement of the GLI for $\lambda_n=0.46$ (a) and (b) and $\lambda_n=0.27$ (c) and (d). (a) and (c) represent the condensation process, while (b) and (d) depict the evaporation process. Additionally, (a)–(c) corresponds to the slip-jump-slip-stick cycle, whereas (d) illustrates the slip-jump-stick cycle.

$$f_e = \frac{\gamma_{sg} - \gamma_{sl}}{\gamma}, \quad f_h = \cos(\theta_a).$$
 (21)

The droplet elastic restoring force is calculated as follows: 31,47,57

$$f_e = k_a \Delta R, \tag{22}$$

where k_a is the accurate Hookean spring constant (spring constant) and ΔR represents the deformation of the GLI and is defined as

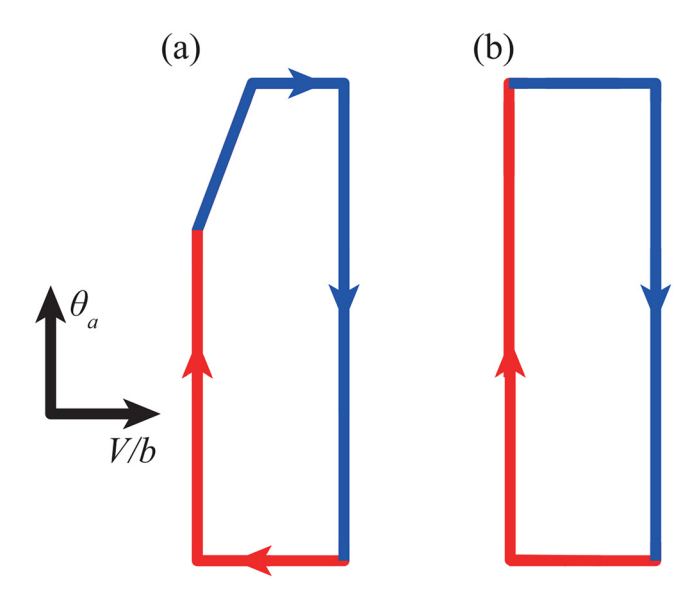


FIG. 6. Schematic diagrams of (a) asymmetric and (b) symmetric CAH loops. In (a), corresponding to Fig. 4(b) within the range $V/b \in [3.0, 5.0]$, the red line represents evaporation and the blue line represents condensation, illustrating an asymmetric loop. In (b), corresponding to Fig. 4(f) within the range $V/b \in [17.4, 19.4]$, the red and blue lines form a symmetric loop.

 $\Delta R = R - R_s$. Here, R_s is the base radius of the undeformed, flat GLI of equal droplet volume.

$$k_{a} = \frac{8\cos^{3}\theta_{a}}{b[\pi - 2\theta_{a} - \sin(2\theta_{a})]}.$$
 (23)

Following Hatipogullari *et al.*,³¹ the spring constant approximation $k \simeq k_a$ is valid when the heterogeneity strength is small, i.e., $\varepsilon/2 \ll \cos(\theta_0)$, such that $\theta_a \simeq \theta_0$. Within the parameter range considered in this work, the resulting relative error does not exceed 15% [Fig. 7(a)], and the stability criterion remains consistent. Beyond this range (e.g., $\varepsilon/2 > 0.6$), the approximation will lose further accuracy [see Fig. 7(a)]. k can be calculated as follows:

$$k = \frac{8\cos^3\theta_0}{b[\pi - 2\theta_0 - \sin(2\theta_0)]} \simeq k_a. \tag{24}$$

To better illustrate the conditions and process of the jump mode, this paper compares the jumping contact line to a mass-spring-damper model in an overdamped state [Fig. 7(a)]. The overdamped state is an observed outcome. As shown in Fig. 4, neither the contact line nor the interface exhibits oscillations after a jump, indicating the absence of an underdamped response. This arises because the droplet is quasi-static prior to a jump, with the contact line motion driven solely by evaporation/condensation. Consequently, no significant kinetic energy is present at the onset. Therefore, inertial effects are always negligible, precluding an underdamped response.

In this analogy, the heterogeneity force represents the external force acting on the system, the elastic restoring force corresponds to the spring force, and fluid viscosity serves as the damping force. Our focus is on the instant when the contact line begins to jump and the moment when it completes its jump and stabilizes. The analogy is established from the perspectives of force balance and energy conservation: when the Yang equation holds, the contact line remains stable (sliding or pinning) with elastic energy stored as interfacial deformation, whereas a sharp wettability change disrupts equilibrium, leading to a jump where stored energy is released as fluid kinetic energy before being dissipated by viscosity. Based on this analogy, the contact line's stability criterion can be concluded that

$$\begin{cases} k > \mathrm{d} \cos[\theta_a(R)]/\mathrm{d}R, & \mathrm{Stability}, \\ k = \mathrm{d} \cos[\theta_a(R)]/\mathrm{d}R, & \mathrm{Criticality}, \\ k < \mathrm{d} \cos[\theta_a(R)]/\mathrm{d}R, & \mathrm{Jump}. \end{cases}$$
 (25)

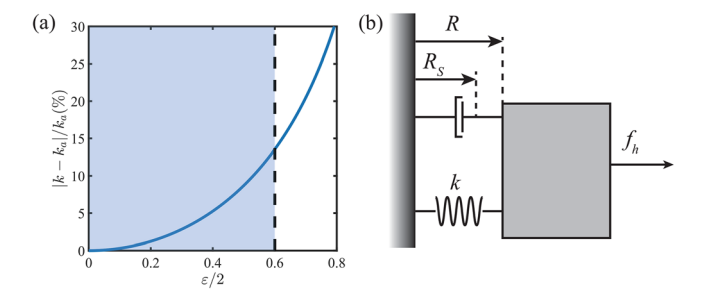


FIG. 7. (a) is the evaluation of the accuracy of approximation. (b) is the schematic diagram for the mass–spring–damper model, which is the analogue of contact line jump.

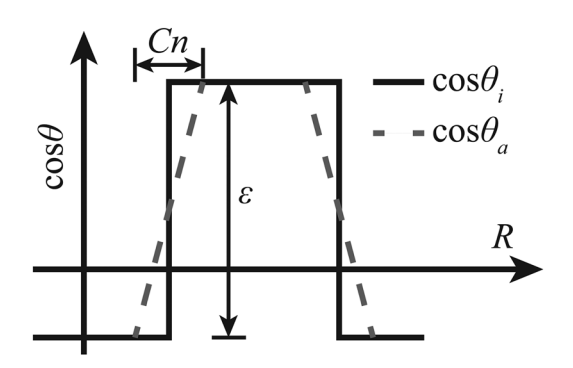


FIG. 8. The comparison diagram of inherent contact angle θ_i and apparent contact angle θ_a when using the LCB Eq. (5) to handle θ_a in the transition region with width Cn.

The detailed derivation and validation of the stability criterion are presented in Appendix C. In the following, we further clarify the calculation of the heterogeneity force gradient for mesa defects. In our analytical solutions, the apparent contact angle θ_a of the mesa defect is determined using the LCB equation [Eq. (5); see Fig. 8]. It is important to note that within the transition region of mesa defects, $\theta_a(R) \neq \theta_i(R)$. The width of this transition region is given by Cn, and within this region, the heterogeneity force gradient is $\pm \varepsilon/Cn$. Therefore, the analytical expression for heterogeneity force gradient is

$$\frac{\mathrm{d}\cos(\theta_a)}{\mathrm{d}R} = \sum_{n} \left\{ \Pi[R - (n+1/2) + \lambda] - \Pi(R - n) \right\}, \quad n \in \mathbb{Z},$$
(26a)

$$\Pi(x) = \begin{cases} \varepsilon/Cn & |x| \le Cn/2, \\ 0 & |x| > Cn/2. \end{cases}$$
 (26b)

The combination of Eqs. (26b) and (24) reveals the parameters that affect the contact line jump in the microchannel with mesa defects: reference contact angle θ_0 , microchannel width b, heterogeneity strength ε , and Cahn number Cn. By setting the parameters properly, all cases in this paper meet $\min(\varepsilon/Cn) > \max(k)$, which ensures the occurrence of contact line jump.

C. Discussion of CAH

This section focuses on deriving the relationship between CAH, H, and energy dissipation, W, in a microchannel with heterogeneity defects. This formula is the foundation of the CAH model proposed in this study. To accomplish this, we extend and adapt the model developed by Joanny and de Gennes, making it applicable to a broader range of scenarios and ensuring its relevance to more general cases.

Building on the previous analysis, the behavior of the contact line is primarily governed by the interplay between the heterogeneity force and the elastic restoring force. Figure 9 provides a graphical representation of this force balance to illustrate their influence on MCL. In this construction, the comparison between the gradient of the heterogeneity force, $d\cos[\theta_a(R)]/dR$, and the spring constant k is reduced to a comparison of the slopes of a straight line (representing the elastic restoring force, f_e) and the tangent to a curve (representing the heterogeneity force, f_h). At points a and e, the contact line can return to a

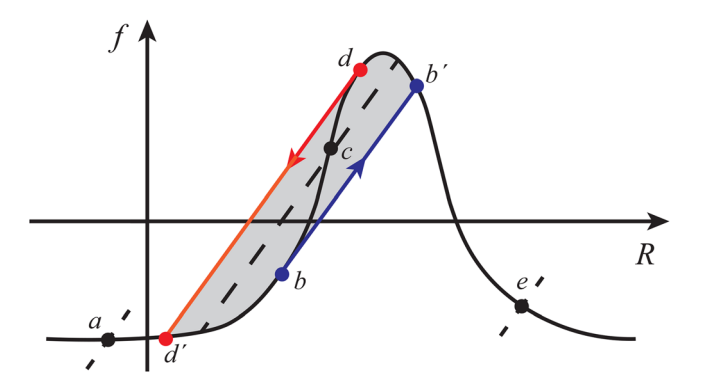


FIG. 9. Graphical representation of force balance during contact line jumps. The blue and red lines depict the contact line trajectories during condensation and evaporation, respectively. The dashed line represents the elastic restoring force (f_e) , while the solid black line represents the heterogeneity force (f_h) . Points b and d indicate the tangency points between the elastic restoring force and heterogeneity force curves.

stable state after a small disturbance. However, at point c, the contact line cannot maintain stability. The critical points b and d correspond to the bifurcation points in Figs. 4(e) and 4(f). When the contact line reaches these points, it jumps to the next stable state, transitioning to d' or b' depending on the direction of motion.

This graphical construction clearly outlines the trajectory and behavior of the contact line. For instance, starting from point a and moving to the right through the defect (representing droplet condensation), the contact line follows the path $a \to d' \to b \to b' \to e$. This trajectory corresponds to the condensation curve in Fig. 4, with changes in the heterogeneity force aligning with the advancing contact angle, θ_A . Conversely, starting from point e and moving left through the defect (representing droplet evaporation), the path is $e \to b' \to d \to d' \to a$. This trajectory corresponds to the evaporation curve, with changes in the heterogeneity force representing the receding contact angle, θ_R .

The contact line jump creates distinct, non-overlapping trajectories during evaporation and condensation, leading to CAH: $H \neq 0$. In addition, the viscosity can cause energy dissipation W during jumping. In Appendix D, we have theoretically derived and proven the relationship between H and W based on energy conservation. In this process, jump leads the stored energy to be released as fluid kinetic energy before being dissipated by viscosity. The result is as follows:

$$H = W. (27)$$

In Appendix D, it was established that *H* represents the area of the shaded region in Fig. 9. This forms the foundation for the CAH model proposed in this study, which calculates CAH directly through a graphical representation of force balance. Before delving into this model, it is essential to analyze the CAH modes.

In Chang *et al.*'s⁴⁷ pioneering study on CAH in microchannels, two CAH modes were identified: Individual-Effect-Dominated Hysteresis (IDH) and Collective-Effect-Dominated Hysteresis (CDH). As shown in Figs. 10(a) and 10(c), CDH occurs when the contact line transitions directly between defects without intermediate slipping, meaning individual defects have minimal impact, and collective defects dominate the contact line behavior. Conversely, IDH is characterized

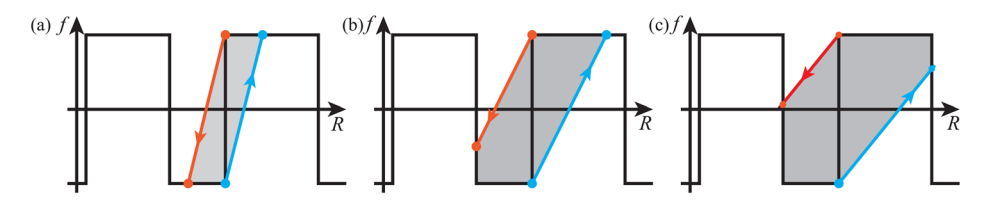


FIG. 10. Schematic diagram of CAH modes with mesa. The blue line represents the trajectory of the contact line jump during condensation, and the red line represents the trajectory during evaporation. Among them, (a) is the IDH mode, (b) is the HDH mode, and (c) is the CDH mode.

by a slip-jump-slip-stick cycle, where individual defects significantly influence the contact line.

In the original study, the CAH mode was symmetric, with identical contact line jumping behavior during evaporation and condensation, attributed to their specific cases with $\lambda=0.5$ (equal-width patterned heterogeneity). This paper explores a novel asymmetrical CAH mode with $\lambda\neq0.5$ (non-equal-width patterned heterogeneity). Figure 10(b) shows that the contact line exhibits distinct jumping behaviors during evaporation and condensation. This new mode, termed hybrid-effect-dominated-hysteresis (HDH), has been validated through MCMP-LBM simulations (Fig. 4).

The criteria for the type of CAH consist of two parts: the jumping behavior and the symmetry/asymmetry of the contact line. For example, in a microchannel with specific heterogeneity, if the contact line can stop in the background or the defect, after jumping during evaporation and condensation, we define that the CAH in this case is symmetrical and refer to it as IDH, referring to Fig. 10(a). The definition of CDH is similar, meaning that during evaporation and condensation, the contact line can stop in the transition area between the background and the defect after jumping, referring to Fig. 10(c). HDH is a newly discovered particular case. In this situation, CAH is not symmetrical. For instance, the contact line can jump to the transition area during evaporation. Still, it can only jump to the defect or the background during condensation, referring to Fig. 10(b). This asymmetric behavior cannot be classified by existing IDH/CDH criteria, 47 which only

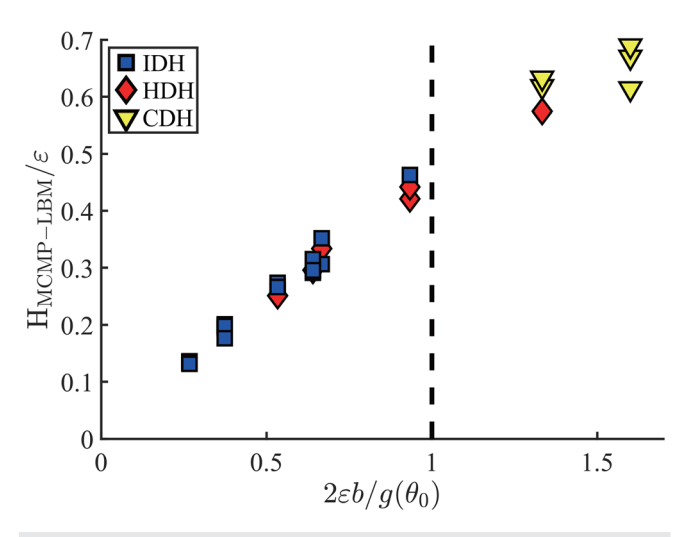


FIG. 11. The classification of contact angle hysteresis (CAH) modes based on theory from Chang *et al.*, ⁴⁷ while $2\varepsilon b/g(\theta_0)=1$ presents the criterion for distinguishing between modes IDH and CDH.

capture symmetric processes (Fig. 11). We, therefore, regard HDH as a distinct mode.

The CAH mode can be identified using the graphical force method by analyzing the intersection of the contact line jump trajectory with the heterogeneity force curve in Fig. 12. In the non-equal width case (λ_n < 0.5), the background is significantly wider than the defect. Thus, during condensation, the contact line may lack sufficient capability to cross the wide background and becomes arrested in a stable region, while during evaporation, it can readily jump across the much narrower defect, landing in the transition zone. These processes are illustrated in Fig. 12(b). Based on the above-mentioned analysis, we construct the criteria including "Evaporation criterion" (Ec) and "Condensation criterion" (Cc) to predict the symmetry of MCL in each defect, respectively. This asymmetry is quantified by the Ec and Cc parameters: Ec (evaporation) and Cc (condensation) measure how strongly the background and defect widths constrain the jump position. As summarized in Fig. 12, their signs provide a unified criterion distinguishing IDH (Ec < 0, Cc < 0), CDH (Ec > 0, Cc > 0), and HDH (Ec > 0, Cc < 0). Appendix E presents a detailed derivation of this approach, and the result is

$$Ec \equiv \frac{b\varepsilon}{g(\theta_0)} - \lambda_n, \tag{28a}$$

$$Cc \equiv \frac{b\varepsilon}{g(\theta_0)} - (1 - \lambda_n),$$
 (28b)

$$g(\theta_0) \equiv \frac{8\cos^3\theta_0}{\pi - 2\theta_0 - \sin(2\theta_0)}.$$
 (28c)

In this criteria, the signs of (Ec) and (Cc) reflect the modes of droplet during evaporation and condensation: when Ec>0, the droplet undergoes CDH; when Ec<0, the droplet undergoes IDH. The same goes for Cc. The consistency of signs reflects the symmetry of CAH modes. Through the combination of criteria, we can distinguish the CAH modes in microchannels with mesas:

- Ec < 0 and Cc < 0: **IDH**.
- Ec > 0 and Cc > 0: **CDH**.
- Ec > 0 and Cc < 0: **HDH**.

The Ec-Cc framework serves as a mapping from the parameters of a heterogeneous microchannel (e.g., b, ε , and λ_n) to the corresponding CAH mode. We keep the arrangement of λ_n using Eq. (18) and calculate each CAH during evaporation and condensation. By plotting Ec on the horizontal axis and Cc on the vertical axis, the CAH mode can be identified based on the quadrant in which the case falls, as illustrated in Fig. 13. Furthermore, using the definitions of Ec and Cc, along with the H-W relationship described in Eq. (28b), we derive an equation for predicting CAH in microchannels containing mesa defects

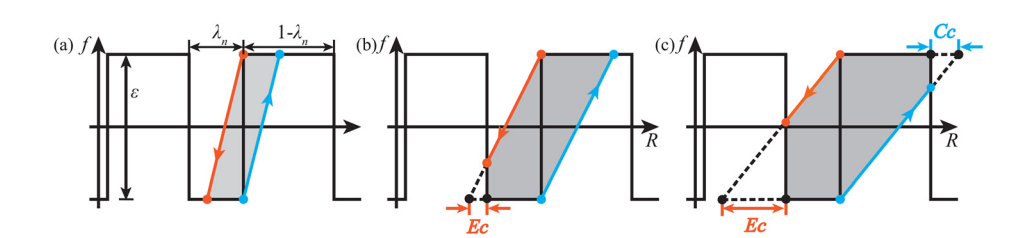


FIG. 12. Schematic diagram of *Ec* and *Cc* in different CAH modes with mesa. Among them, (a) is the IDH mode, (b) is the HDH mode, and (c) is the CDH mode.

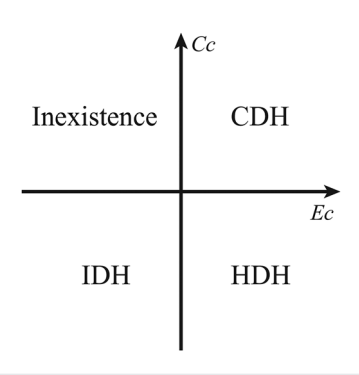


FIG. 13. The phase diagram used to determine the CAH modes.

$$H = \frac{b\varepsilon^2}{g} - \frac{g}{2b} \left[h(Ec)Ec^2 + h(Cc)Cc^2 \right], \tag{29a}$$

$$h(x) = \begin{cases} 1, & x > 0, \\ 0, & x \le 0. \end{cases}$$
 (29b)

The detailed derivation process is provided in Appendix F. Verification using MCMP-LBM simulations is presented in Fig. 14. As shown, all data points corresponding to different modes are correctly positioned in their respective quadrants in panel (a) and collapse onto a single curve in panel (b), aligning well with the theoretical predictions.

V. THREE-DIMENSIONAL RESULTS AND DISCUSSION A. Setting

The physical description of the 3D cases is provided in Sec. II A. Compared to the 2D scenarios, the 3D cases introduce an additional parameter, λ_y , which controls the lateral heterogeneity. The physical significance of λ_y lies in influencing the contact line's lateral

deformation. When $0 < \lambda_y < 1$, this deformation can lead to deviations in CAH from the predictions of Eq. (29b). Consequently, simulations of the 3D cases are conducted to refine and enhance the CAH model for heterogeneous microchannels.

In the 3D cases, the local apparent contact angle depends on the spatial variation along the *y*-direction for a given contact line shape, represented as $\theta_a = \theta_a(y)$. The spatially averaged apparent contact angle is expressed as

$$\theta_{ave} = \int_{0}^{1} \theta_{a}(y) dy, \tag{30}$$

$$R_{ave} = \int_0^1 R(y) \mathrm{d}y. \tag{31}$$

B. Result

The MCMP-LBM simulation results are shown in Fig. 15. Consistent with the 2D simulation, the results exhibit a typical cycle of MCL: (a)-(c) and (e) and (f) represent the stick phase, (c) and (d) represents slip, and (d) and (e) represents jump. When the contact line is in the background, it remains straight, similar to the 2D case. However, when the contact line encounters defects, it becomes distorted, leading to wrinkling and deformation of the GLI near the wall surface. The effect of this deformation on contact line behavior is shown in Figs. 15(g) and 15(h). The contact line deformation causes a significant discrepancy between the actual average contact angle and the wettability of the defect when the contact line is positioned on the defect. Therefore, relying solely on parameters θ_0 and ε is insufficient to characterize heterogeneous microchannels' wettability fully. Additional parameters related to the arrangement of 3D defects, such as λ_{ν} , must also be considered. This highlights a key difference between the 3D and 2D cases. As a result, conclusions drawn from 2D models must be adjusted to account for the complexities of 3D cases.

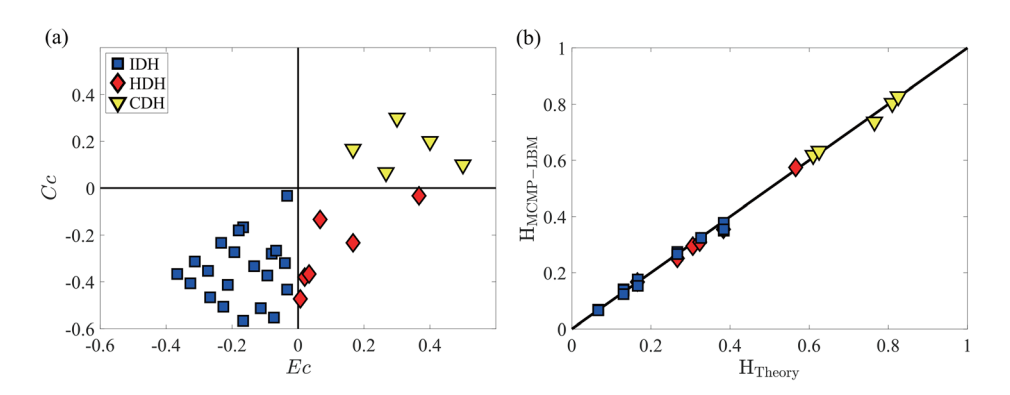


FIG. 14. Verification of (a) the Ec-Cc criterion and (b) theoretical CAH using MCMP-LBM simulations. Each point represents a CAH process in the non-uniform patterned heterogeneity microchannel. The CAH mode is determined directly from the evaporation/condensation curve (Fig. 4), and the coordinates of the points are calculated using Eq. (28b). $H_{\rm MCMP-LBM}$ and $H_{\rm Theory}$ are obtained from Eqs. (19) and (29b), respectively.

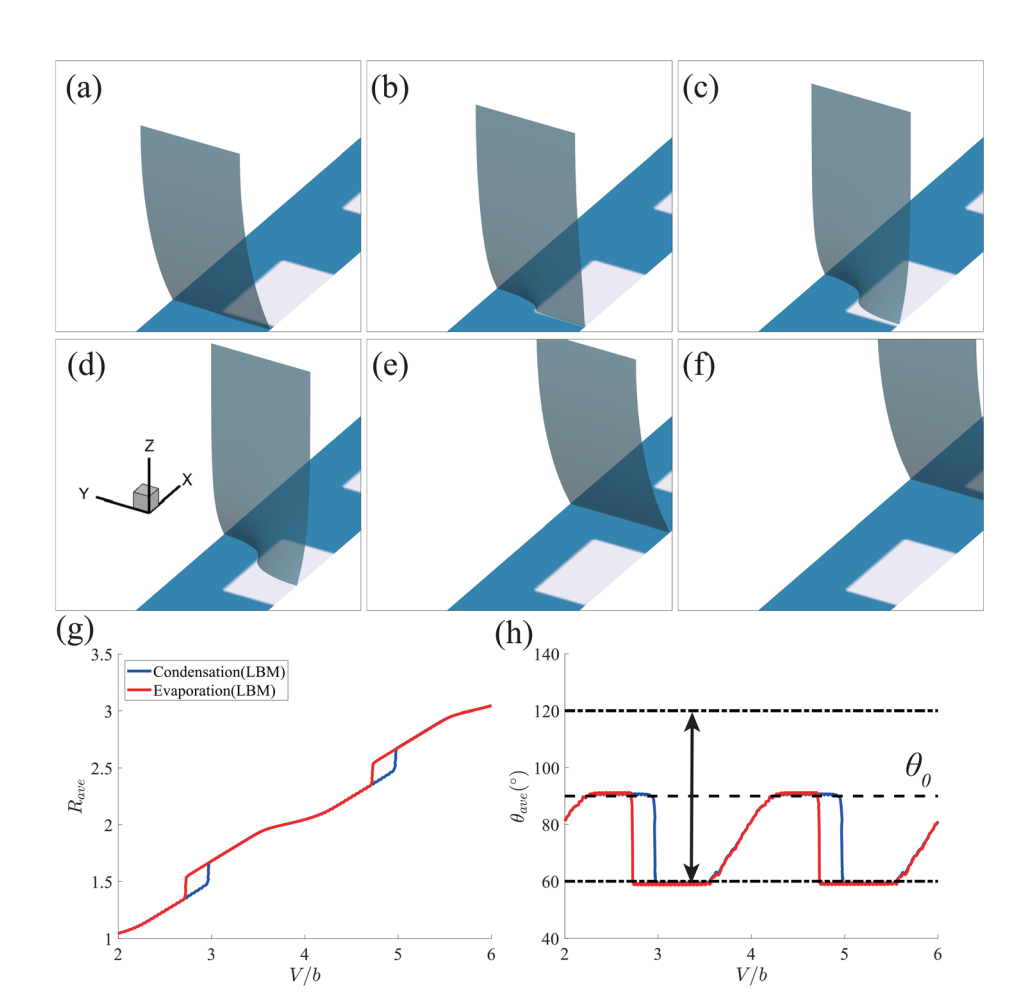


FIG. 15. Evolution of the GLI of the droplet during condensation with parameters b=2, $\lambda_n=0.5$, $\lambda_y=0.5$, $\theta_0=90^\circ$, and $\epsilon=1$. Only the right side of the lower half of the droplet in the microchannel is shown (with the left side representing the liquid phase). (g) and (h) display the behavior of the contact line. The dotted and dashed lines indicate the reference contact angles, background wettability, and defect wettability.

C. Analysis

By capturing the maximum and minimum deformations of the GLI, we can assess the impact of contact line deformation on the GLI. As shown in Fig. 16, the deformation caused by the contact line is localized (close to the wall), with the GLI remaining wrinkle-free away from the upper and lower walls, which aligns with findings from similar research by Chang *et al.*⁴⁷ The average contact angle when the

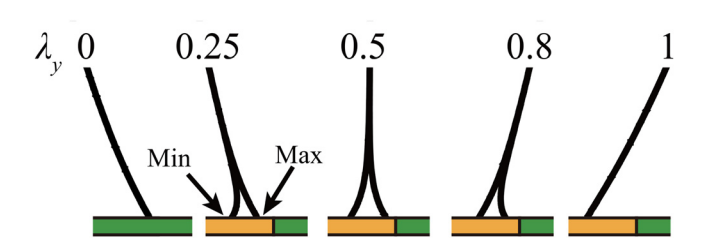


FIG. 16. Side view along the *y*-direction showing the maximum and minimum GLI deformations when the contact line is located on defects under different λ_y conditions. The image is a close-up of the area near the solid wall.

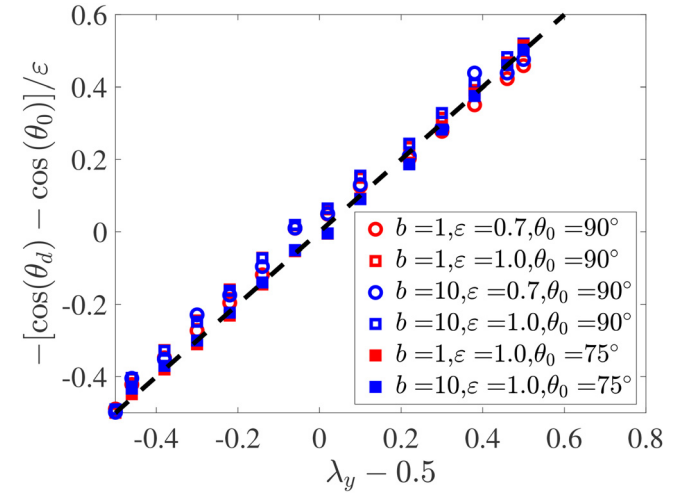


FIG. 17. The linear relationship between θ_d and λ_y after being normalized.

contact line is located on a defect, denoted as θ_d , and its variation trend is presented in Fig. 17, demonstrating the independence of θ_d from b. Furthermore, a quantitative relationship between θ_d and other parameters was derived through linear fitting as follows:

$$-\frac{1}{\varepsilon}[\cos(\theta_d) - \cos(\theta_0)] = \lambda_y - 0.5. \tag{32}$$

Therefore, based on the definitions of θ_0 and ε , we have redefined the modified heterogeneity strength ε' and reference contact angle θ'_0 ,

$$\varepsilon' = \cos \theta_0 + \varepsilon/2 - \cos \theta_d, \tag{33a}$$

$$\cos \theta_0' = \frac{\cos \theta_0 + \varepsilon/2 + \cos \theta_d}{2},\tag{33b}$$

$$\cos \theta_d = \cos \theta_0 - \varepsilon (\lambda_y - 0.5). \tag{33c}$$

The linear relationship in Eq. (33c) is semi-empirical, obtained from observations of interfacial deformation. The modified parameters, calculated from θ_0 and ε , can be directly substituted into analytical or theoretical calculations, effectively transforming the 3D problem into a simpler 2D one. As discussed earlier, we use analytical methods to validate the contact line trajectory obtained from MCMP-LBM simulations. Figure 18 shows good agreement between the simulation and analytical predictions, except during the sticking phase, where the defect's spanwise characteristics cause a deviation. As shown in Fig. 15, when the contact line approaches the defect, part of it behaves like the 2-D case, sticking at the junction, while the rest moves without heterogeneous force variation. This inconsistency causes deformation and leads to spanwise non-uniformity in θ_a and R during the slip process. Even after averaging [as defined in Eqs. (30) and (31)], the parameters

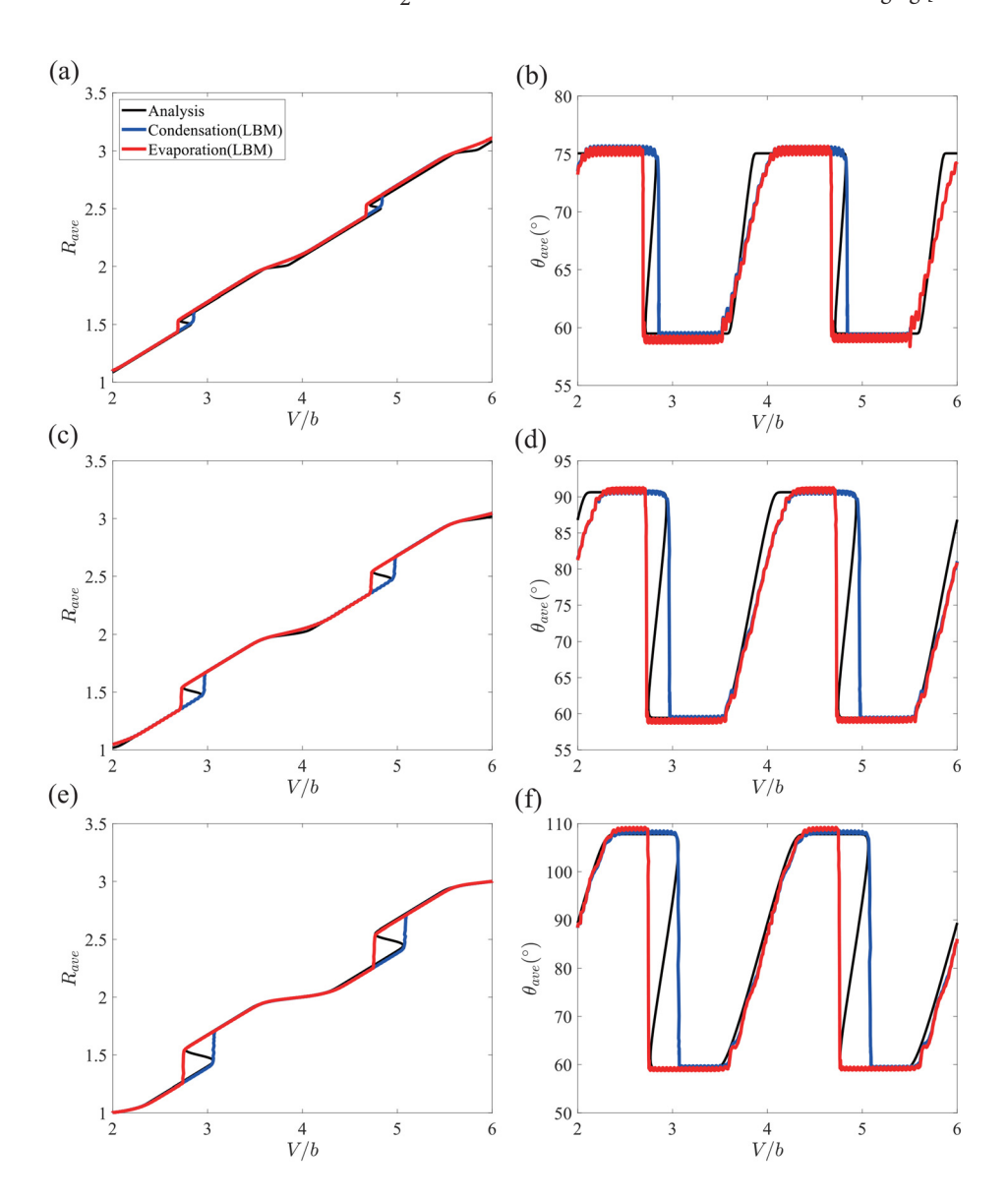


FIG. 18. The behavior of the contact line simulated by MCMP-LBM, compared with the analytical results. The parameter values are $\theta_0=90^\circ$, $\varepsilon=1.0$, b=2, and $\lambda_n=0.5$. Panels (a) and (b) correspond to the case with $\lambda_y=0.25$, (c) and (d) with $\lambda_y=0.5$, and (e) and (f) with $\lambda_y=0.8$.

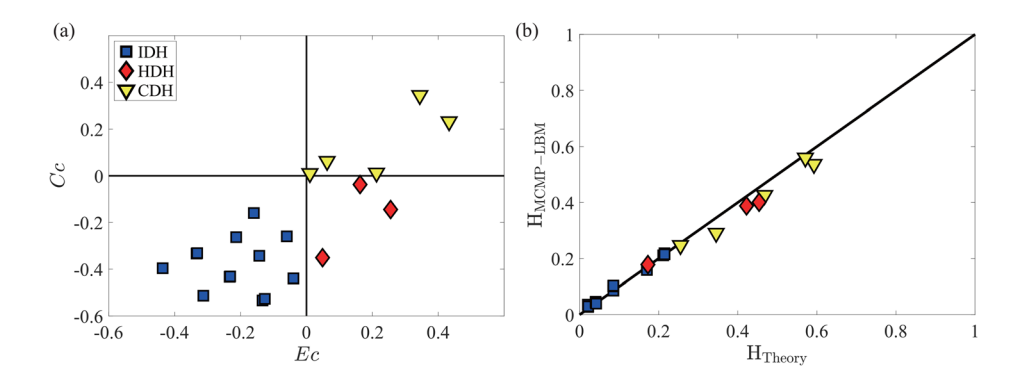


FIG. 19. Verification of the (a) Ec-Cc criterion and (b) theoretical CAH based on MCMP-LBM simulation for 3D cases.

reflecting contact line behavior still show significant differences compared to the 2D case. Jump remains the only mode that causes curve bifurcation in the 3D cases. Similar to the 2D simulation, we keep the arrangement of λ_n using $\lambda_n \in [0.3, 0.4, 0.5]$ and calculate each CAH during evaporation and condensation. Our LBM simulation results align closely with the predictions of the proposed Ec - Cc criterion [see Fig. 19(a)]. The average contact angle $\theta_{\rm ave}$, used to calculate H, is compared with the theoretical predictions in Fig. 19(b), showing excellent agreement between the two. This consistency verifies that, by redefining the modified heterogeneity strength ε' and reference contact angle θ'_0 , the theoretical framework developed for 2D cases (IV) can be effectively extended to 3D scenarios.

VI. CONCLUSIONS

This study provides a comprehensive simulation of evaporation and condensation in heterogeneous microchannels, develops a physical model for contact line jumping, and establishes criteria and calculation formulas for CAH applicable to 2-D and 3-D cases.

Using the MCMP-LBM framework, we accurately simulated contact line behavior and validated the results against analytical predictions. Consistent with prior studies, contact line behavior exhibits a cyclic pattern of three fundamental modes: slip, jump, and stick. Jumping introduces bifurcations in evaporation and condensation curves, leading to CAH. By drawing an analogy between the contact line jumping process and a mass-spring-damper system, we derived macroscopic conditions for contact line jumping based on force balance. The graphical construction of this balance further revealed that CAH is fundamentally equivalent to energy dissipation during the jumping process.

For the representative case of mesa defects, we proposed the Ec-Cc criterion, which accurately identifies three types of CAH, including hybrid-effect-dominated-hysteresis (HDH) resulting from non-equal-width, as discovered in this study. Moreover, our analysis demonstrates that with minor adjustments, the proposed model can be effectively extended to analyze and compute 3-D scenarios, offering a unified framework for understanding CAH in heterogeneous microchannels.

Despite the valuable insight provided by our research, several limitations should be acknowledged: (a) Quasi-steady state assumption. We assume droplet volume changes are driven solely by density differences without external forces, which excludes scenarios with moving droplets driven by kinetic energy or external work. (b) Rectangular heterogeneous patches. 3D simulations model heterogeneities as rectangular patches. Non-rectangular shapes cannot be directly

characterized using the parameters λ_n and λ_y , so the current extension methodology may not apply.

In the final part of our work, we provide suggestions for future research. Our study differ fundamentally from the sessile droplet configurations widely used in existing CAH experiments. Consequently, relevant experimental data are currently unavailable. We suggest that future studies carefully address challenges, mainly are maintaining strict substrate symmetry and avoiding external perturbations. Our results indicate that droplets in such systems are extremely sensitive: even slight asymmetry or disturbance can induce irreversible lateral motion, complicating experimental measurement.

ACKNOWLEDGMENTS

This work was supported by the Natural Science Foundation of China (NSFC) (Grant No. 12372253).

Calculations are performed at the Supercomputing Center of the University of Science and Technology of China.

AUTHOR DECLARATIONS Conflict of Interest

The authors have no conflicts to disclose.

Author Contributions

Heng-yu Hu: Conceptualization (equal); Data curation (equal); Formal analysis (equal); Investigation (equal); Methodology (equal); Software (equal); Visualization (equal); Writing – original draft (equal). Hai-bo Huang: Conceptualization (equal); Formal analysis (equal); Funding acquisition (equal); Investigation (equal); Methodology (equal); Supervision (equal); Writing – review & editing (lead).

DATA AVAILABILITY

The data that support the findings of this study are available from the corresponding author upon reasonable request.

APPENDIX A: GRID INDEPENDENCE STUDY

To ensure numerical consistency, grid resolution is controlled by the parameter β , which represents the number of lattice cells across a characteristic length. The definition of β is shown in Fig. 1. The relevant dimensionless groups [Eq. (A1)] and normalized

physical quantities [Eq. (A2)] are preserved across grid refinements as follows:

$$Re = \frac{U_c \beta}{\nu^{\sigma}}, \tag{A1a}$$

$$Pe = \frac{U_c \beta}{D}, \tag{A1b}$$

$$Ca = \frac{\rho^{\sigma} \nu^{\sigma} U_c}{\gamma}, \qquad (A1c)$$

$$Cn = \frac{\xi}{\beta}, \tag{A1d}$$

$$b^* = \frac{b}{\beta},\tag{A2a}$$

$$R^* = \frac{R}{\beta},\tag{A2b}$$

$$V^* = \frac{V}{\beta^2},\tag{A2c}$$

$$E^* = \frac{E}{\beta \gamma}.$$
 (A2d)

We tested three resolutions: $\beta = 20$, $\beta = 40$, and $\beta = 50$. Convergence was assessed by monitoring droplet jumping behavior (changes in the base radius *R* and volume *V*).

2D (D2Q9): Results (Fig. 20) show that $\beta = 40$ and $\beta = 50$ produce nearly identical behaviors, while $\beta = 20$ exhibits nonphysical effects (e.g., spurious volume loss), confirming that finer grids yield stable results.

3D (D3Q19): A similar trend is observed (Fig. 21); nonphysical artifacts diminish as β increases, and convergence is reached for $\beta > 40$.

These results demonstrate that our simulations are gridindependent at $\beta=40$ or higher, ensuring both accuracy and reliability of the reported findings.

APPENDIX B: WETTABILITY CONDITIONS AND VALIDATION

To simulate the conditions accurately, we implemented the surface energy method developed by Fakhari and Bolster⁶¹ and

further refined by Chang *et al.*⁴⁷ This method is easy to implement and can accurately simulate the contact angle under a quasi-steady state.

Figure 22 illustrates the wetting condition setup. As an initial step, the order parameter $\varphi^{\sigma}(\mathbf{x})$ is calculated based on the density as follows:

$$\varphi^{\sigma}(\mathbf{x}) = \frac{\rho^{\sigma}(\mathbf{x}) - \rho^{\min}}{\rho^{maj} - \rho^{\min}}.$$
 (B1)

Using the finite difference method to discretize the derivative, then the wetting condition is expressed as

$$\mathbf{n}_{w} \cdot \nabla \varphi^{\sigma}|_{\mathbf{x}_{w}} = \frac{\varphi^{\sigma}(\mathbf{x}_{f}) - \varphi^{\sigma}(\mathbf{x}_{s})}{s + h} = -\frac{4}{\lambda} \Theta \varphi^{\sigma}(\mathbf{x}_{w})[1 - \varphi^{\sigma}(\mathbf{x}_{w})]. \tag{B2}$$

The order parameter at wall point \mathbf{x}_w can be obtained through

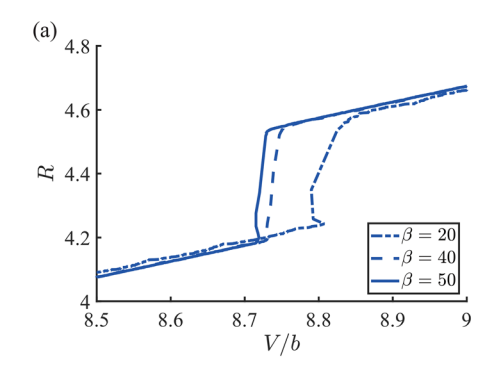
$$\varphi^{\sigma}(\mathbf{x}_{w}) = \frac{h\varphi^{\sigma}(\mathbf{x}_{s}) + s\varphi^{\sigma}(\mathbf{x}_{f})}{s+h}.$$
 (B3)

Substituting Eq. (B3) into (B2), we have

$$\varphi^{\sigma}(\mathbf{x}_{s}) = \begin{cases} \frac{s+h}{2hm} \left[1 + m - \sqrt{(1+m)^{2} - 4m\varphi^{\sigma}(\mathbf{x}_{f})} \right] \\ -\frac{s}{h} \varphi^{\sigma}(\mathbf{x}_{f}), & \theta_{i} \neq 90^{\circ}, \\ \varphi^{\sigma}(\mathbf{x}_{f}), & \theta_{i} = 90^{\circ}, \end{cases}$$
(B4)

where $m=-(4h/\xi)\Theta$. $\Theta=\cos(\theta_i)$ for component σ and $\Theta=\cos(\pi-\theta_i)$ for component $\bar{\sigma}$. To ensure compatibility with the halfway bounce-back scheme, we set h=s=0.5. Consequently, the heterogeneity of the microchannel is fully defined once the arrangement of the inherent contact angle θ_i on the surface is specified.

To further demonstrate the reliability of our numerical method, we have added validation cases. According to both our study and previous work, 47 the interface shape in two dimensions can be well approximated by a standard meniscus, meaning that the interface can be accurately characterized by these two parameters: radius R and central radius R_c , which are shown in Fig. 23(a). Specifically, we suppressed phase change by initializing droplets under equilibrium density conditions and varied substrate wettability to compare base radius R and central radius R_c with analytical



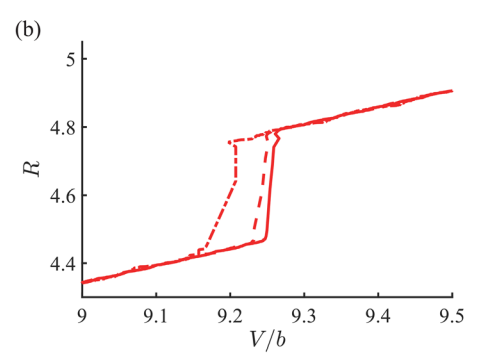
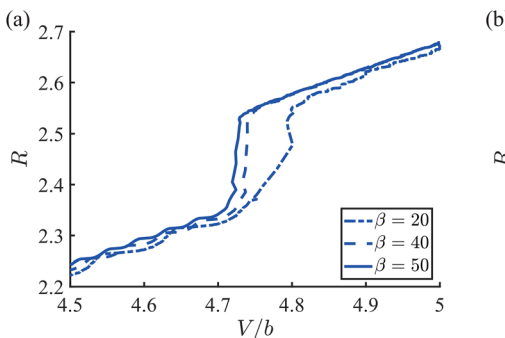


FIG. 20. Grid independence test for 2D (D2Q9) simulations at three resolutions ($\beta=20,40,50$). (a) Condensation and (b) evaporation cases. Results show convergence between $\beta=40$ and $\beta=50$, while $\beta=20$ exhibits spurious artifacts (e.g., volume loss). In the cases, b=4, $\varepsilon=0.5$, and $\lambda=0.5$.



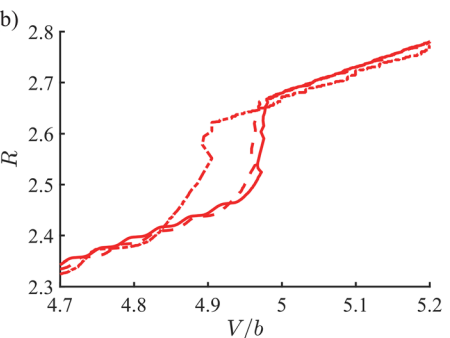


FIG. 21. Grid independence test for 3D (D3Q19) simulations at three resolutions ($\beta=20,40,50$). (a) Condensation and (b) evaporation cases. Similar to the 2D results, convergence is reached for $\beta\geq40$, while coarse grids produce non-physical behavior. In the cases, b=4, $\varepsilon=0.5$, $\lambda_{\gamma}=0.5$, and $\lambda=0.5$.

predictions. Based on the mass (volume) conservation of the droplet, we derived the relationships between the parameters R_c and R and the apparent contact angles θ_a . As shown in Fig. 23, the numerical results are in excellent agreement with analytical solutions in the following, reinforcing the accuracy of our method. This validation is based on quasi-static rather than dynamic conditions.

$$R = \frac{V}{2b} - b \cdot \frac{2\theta_{a} - \pi + \sin(2\theta_{a})}{8\cos^{2}(\theta_{a})},$$

$$R_{c} = R - b \cdot \frac{1 - \cos(\pi/2 - \theta_{a})}{2\sin(\pi/2 - \theta_{a})}.$$
(B5)

APPENDIX C: THE CONTACT LINE'S STABILITY CRITERION

At a specific position R, the heterogeneity force and the elastic restoring force on the contact line are balanced, such that $f_h(R) - f_e(R) = 0$. When a small perturbation occurs, it causes the contact line to shift by a small displacement R_ϵ ($0 < R_\epsilon \ll 1$), while the droplet volume remains constant. To return to its original state after the disturbance, the contact line must satisfy the following conditions:

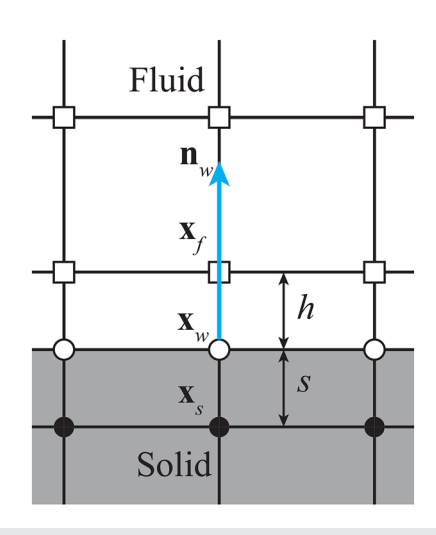


FIG. 22. Schematic diagram for the implementation of wetting condition.

$$f_h(R+R_\epsilon) - f_e(R+R_\epsilon) < 0$$
 and $f_h(R-R_\epsilon) - f_e(R-R_\epsilon) > 0$. (C1)

Substituting the equilibrium condition, Eq. (C1) is equivalent to

$$\frac{f_h(R \pm R_{\epsilon}) - f_h(R)}{\pm R_{\epsilon}} - \frac{f_e(R \pm R_{\epsilon}) - f_e(R)}{\pm R_{\epsilon}} < 0.$$
 (C2)

Since the volume of the droplet does not change during the disturbance, R_s remains constant. Therefore, $[f_e(R\pm R_\epsilon)-f_e(R)]/\pm R_\epsilon=k$. Let $R_\epsilon\to 0$ and use the definition of the derivative to obtain the stability criterion for contact line as follows:

$$\begin{cases} k > \mathrm{d} \cos[\theta_a(R)]/\mathrm{d}R, & \mathrm{Stability}, \\ k = \mathrm{d} \cos[\theta_a(R)]/\mathrm{d}R, & \mathrm{Criticality}, \\ k < \mathrm{d} \cos[\theta_a(R)]/\mathrm{d}R, & \mathrm{Jump}. \end{cases}$$
 (C3)

To compare the spring constant k with the heterogeneity force gradient $d\cos[\theta_a(R)]/dR$, one can determine the jump. If there exists a region where $k < d\cos[\theta_a(R)]/dR$ is satisfied, then the contact line will jump from the critical points.

The microchannel's wettability is constructed using the hyperbolic tangent function to verify the proposed contact line jump criterion's accuracy. The heterogeneity force and its gradient are as follows:

$$\cos[\theta_i(R)] = \cos(\theta_0) + \frac{\varepsilon}{2} \tanh[A_0(R - R_m)], \quad (C4a)$$

$$\frac{\mathrm{d}(\cos\theta_i)}{\mathrm{d}R} = \frac{\varepsilon}{2} A_0 \left\{ 1 - \left[\cos(\theta_i)/\varepsilon\right]^2 \right\},\tag{C4b}$$

where A_0 is a parameter that controls the maximum value of the heterogeneity gradient in the transition region and R_m is the location of the maximum value. It should be noted that the Eq. (C4a) can be used to model the mesa defects' property shown in Fig. 2. The hyperbolic tangent function in Eq. (C4a) effectively controls the gradient of heterogeneity in the transition region, thereby facilitating the study of contact line jumps.

$$\cos \theta_a(R) = \frac{1}{\xi} \int_{R-\xi/2}^{R+\xi/2} [\cos \theta_i(r)] dr.$$
 (C5)

To illustrate how the relative sizes of k and A_0 affect the behavior of the contact line within the microchannel, we present an

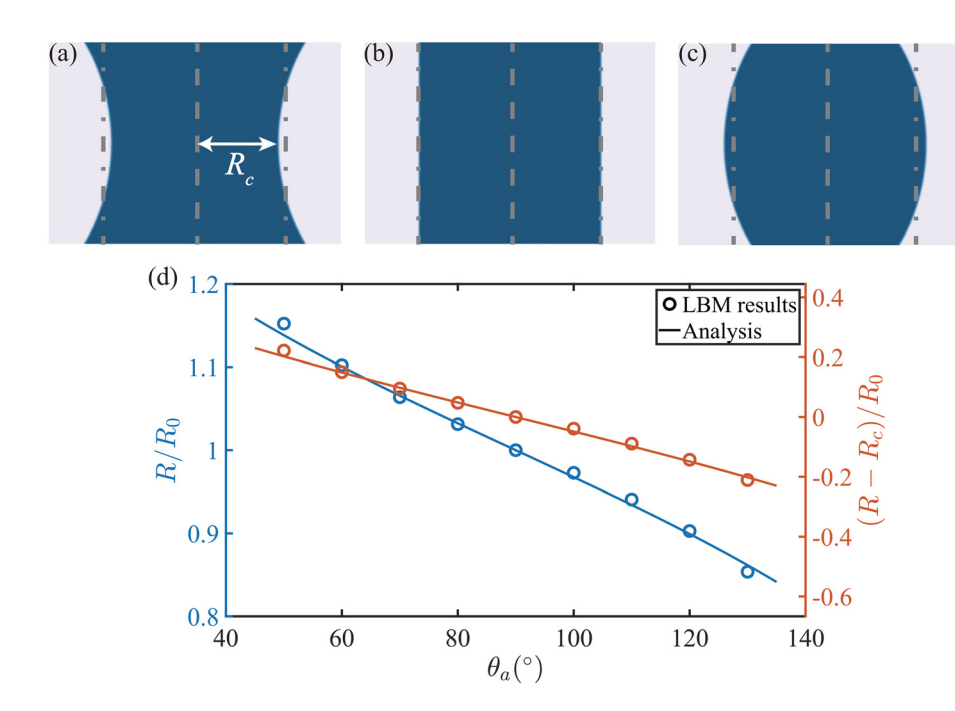


FIG. 23. (a)–(c) Schematic droplet configurations inside the microchannel at apparent contact angles $\theta_a=60^\circ$, 90° , and 120° . (d) Comparison between analytical solutions and numerical results for the base radius R and central radius R_c across different θ_a . The strong agreement confirms the reliability of the proposed numerical method in predicting droplet geometry inside microchannels.

example. Calculate $\theta_a(R)$ using Eq. (C5), a variant of LCB equation [Eq. (5)]. Set $\theta_0 = 90^\circ$, k = 0.5, and $\varepsilon = 0.7$. The results are shown in Fig. 24. In Figs. 24(a)–24(c), the condition $k < d\cos[\theta_a(R)]/dR$ is not satisfied, keeping the contact line in a stable or critical state, and no curve divergence caused by jumps occurs under this condition. In contrast, Figs. 24(d)–24(i) show a different scenario where

jumps occur, with the jump locations coinciding with the critical points (i.e., the intersection of the solid and dashed lines). The misalignment of these critical points leads to curve bifurcation and, ultimately, the emergence of CAH. The simulated results from the MCMP-LBM method confirm the predictions made by Eq. (C4b).

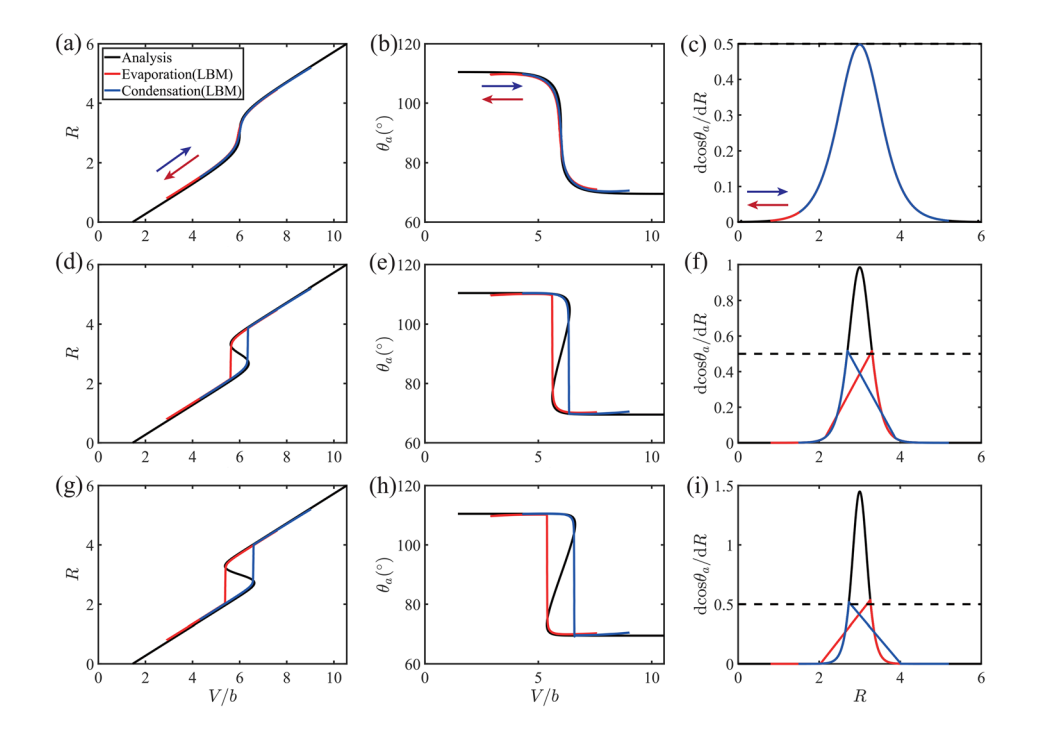


FIG. 24. The contact line jump simulated by MCMP-LBM and the comparison with the analytical method. Cases for (a)–(c) $A_0=0.5$, (d)–(f) $A_0=1.0$, and (g)–(i) $A_0=1.5$. Dashed lines represent k.

APPENDIX D: DERIVATION OF H - W

In the equivalent model discussed earlier (Fig. 7), the behavior of a contact line jump is analogous to the system's response after being perturbed at a critical point. In the absence of damping, the mass-spring system would oscillate indefinitely with constant amplitude, maintaining a constant level of mechanical energy. However, with damping present, the system's mechanical energy is irreversibly converted into thermal energy by the damper, ultimately bringing the system to a new stable state beyond the critical point.

This study applies a similar perspective to analyze CAH. During the transition from a critical point to a stable state, the work done by the resultant force generates kinetic energy. As the contact line reaches stability, all this kinetic energy is gradually dissipated due to the effects of viscosity. By leveraging energy conservation principles, the energy dissipation *W* can be calculated indirectly as the work done by the resultant force during the contact line jump as follows:

$$W = \int_{b}^{b'} (f_h - f_e) dR + \int_{d'}^{d} (f_e - f_h) dR.$$
 (D1)

This indicates that W equals the enclosed area (already marked in gray) surrounded by bb'dd' in Fig. 9. This conclusion can significantly reduce the computational complexity for some special arrangements of heterogeneity defects (such as mesa).

Substitute Eq. (20) into (19) and determine the lower limit of integration $V_0(R_0)$ to get

$$H = \langle \cos \theta_R \rangle - \langle \cos \theta_A \rangle = \frac{1}{2b} \int_{V_0}^{V_0 + 2b} [\cos(\theta_R) - \cos(\theta_A)] \, dV.$$
 (D2)

Using Eq. (2), we can derive that

$$dV = 2bdR + 2bdf, (D3)$$

where $f = b\{[2\theta_a(R) - \pi + \sin 2\theta_a(R)]/8 \cos^2\theta_a(R)\}$. Replace the variable V and the corresponding integration limits in Eq. (D2) with (D3) to obtain

$$H = \int_{R_0}^{R_0+1} (\cos \theta_R - \cos \theta_A) dR +$$
 (D4)

$$\int_{f(R_0)}^{f(R_0+1)} (\cos \theta_R - \cos \theta_A) \mathrm{d}f. \tag{D5}$$

Due to the special arrangement of heterogeneity defects, for any area of unit length, there are only two situations: it contains a complete defect, or it contains two incomplete defects. In either case, f(R) = f(R+1) is satisfied. The integration limits on both sides of the second term on the right side of the Eq. (D5) are the same, causing that term to cancel out as follows:

$$H = \int_{R_0}^{R_0+1} (\cos \theta_R - \cos \theta_A) dR.$$
 (D6)

Equation (D6) also calculates the area of the gray area in Fig. 9, which is entirely consistent with the derivation result of energy

dissipation W. Therefore, in microchannels containing heterogeneity spots, the contact angle hysteresis H and energy dissipation W satisfy the following relationship:

$$H = W. (D7)$$

Equation (27) is derived without distinguishing the specific types of heterogeneity defects. Thus, it has considerable applicability. This paper only conducts validation based on mesa.

APPENDIX E: Ec - Cc DERIVATION

Determining the CAH pattern involves two steps: (1) Analyzing the contact line's jumping behavior during evaporation and condensation and (2) Determining whether the CAH exhibits symmetry.

We use a graphical construction of the force balance to analyze the contact line jumping behavior in a heterogeneous microchannel containing mesa defects, as illustrated in Fig. 25. By comparing the elastic recovery coefficient k with two characteristic slopes (denoted as k_1 and k_2), we can determine the mode of CAH. Given our definition of defects ($0 \le \lambda_n \le 0.5$), the condition $k_2 \le k_1$ is always satisfied. Comparing k and k_1 provides insight into the contact line's behavior during evaporation: When $k > k_1$, the contact line jumps to the defect during evaporation; when $k < k_1$, the contact line jumps to the transition region. The relationship between the magnitudes of k and k_1 can be defined as the sign of Ec,

$$k > k_1 \to b/g(\theta_0) < \lambda_n/\varepsilon \to Ec \equiv b\varepsilon/g(\theta_0) - \lambda_n < 0,$$
 (E1a)

$$k < k_1 \to b/g(\theta_0) > \lambda_n/\varepsilon \to Ec \equiv b\varepsilon/g(\theta_0) - \lambda_n > 0.$$
 (E1b)

A similar analysis can be conducted for the contact line jumping behavior during condensation, resulting in the definition of *Cc*

$$k > k_2 \rightarrow b/g(\theta_0) < (1 - \lambda_n)/\varepsilon \rightarrow Cc \equiv b\varepsilon/g(\theta_0) - 1 + \lambda_n < 0,$$
(E2a)

$$k < k_2 \rightarrow b/g(\theta_0) > (1 - \lambda_n)/\varepsilon \rightarrow Cc \equiv b\varepsilon/g(\theta_0) - 1 + \lambda_n > 0.$$
(E2b)

2. The signs of Ec and Cc indicate the contact line's jumping behavior during evaporation and condensation, respectively. By plotting these two parameters on a phase diagram, we can identify the CAH mode based on the quadrant, as illustrated in Fig. 13. The absence of data in the second quadrant, labeled "Inexistence," arises because, under the defect definition used in this study $(0 \le \lambda_n \le 0.5)$, no scenarios exist where Ec < 0 and Cc > 0. In essence, the Ec - Cc criterion provides a framework to map the parameters characterizing the heterogeneous microchannel (e.g., b, λ_n , θ_0 , etc.) to the corresponding CAH mode.

APPENDIX F: H DERIVATION

We have already demonstrated the relationship between CAH and viscous dissipation (H=W). Therefore, by calculating the area of a specific region in Fig. 26, we can directly determine the H in heterogeneous microchannels with mesa defects. The following will analyze the H for the three CAH modes:

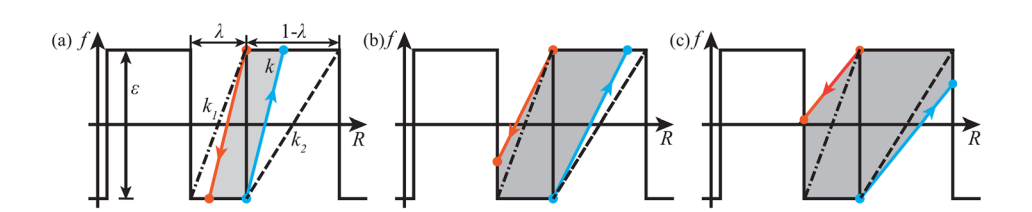


FIG. 25. The graphical construction of the force balance with mesa defects. The definition of characteristic slopes are $k_1 = \varepsilon/\lambda_n$ and $k_2 = \varepsilon/(1-\lambda_n)$. (a), (b), and (c) represent three different contact line jumping modes and their corresponding CAH.

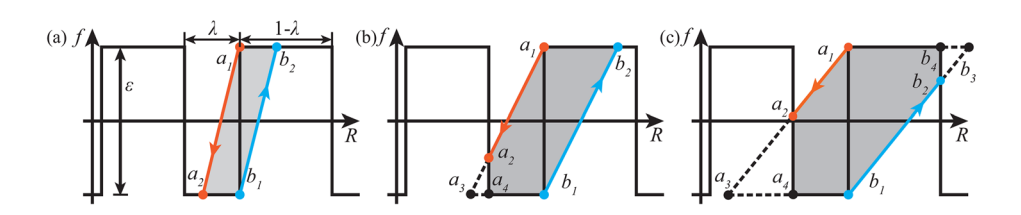


FIG. 26. The graphical construction of the force balance with mesa defects. Among them, (a) is IDH mode, (b) is HDH mode, and (c) is CDH mode, with the dashed line being the extended line of the trajectory. All points of intersection are labeled with letters

1. **IDH.** In Fig. 26(a), H is equivalent to the area $S_{a_1a_2b_1b_2}$ of the parallelogram formed by points a_1 , a_2 , b_1 , and b_2

$$H_{IDH} = S_{a_1 a_2 b_1 b_2} = l_{a_2 b_1} \varepsilon = \frac{b \varepsilon^2}{g(\theta_0)}. \tag{F1}$$

2. **HDH.** In Fig. 26(b), *H* is equivalent to the difference between the area $S_{a_1a_2b_1b_2}$ of the parallelogram and the area of left triangle $S_{a_2a_3a_4}$:

$$H_{HDH} = \frac{b\varepsilon^2}{g(\theta_0)} - \frac{g(\theta_0)}{2b} \left[\frac{b\varepsilon}{g(\theta_0)} - \lambda_n \right]^2.$$
 (F2)

Substituting the definition of Ec (E1b) into Eq. (F2), it simplifies to

$$H_{HDH} = \frac{b\varepsilon^2}{g(\theta_0)} - \frac{g(\theta_0)}{2b} Ec^2.$$
 (F3)

3. **CDH.** In Fig. 26(c), H is equivalent to the difference between the area $S_{a_1a_2b_1b_2}$ of the parallelogram, the left triangle $S_{a_2a_3a_4}$ and the right triangle $S_{b_2b_3b_4}$,

$$H_{CDH} = \frac{b\varepsilon^2}{g(\theta_0)} - \frac{g(\theta_0)}{2b} \left[\frac{b\varepsilon}{g(\theta_0)} - \lambda_n \right]^2 - \frac{g(\theta_0)}{2b} \left[\frac{b\varepsilon}{g(\theta_0)} - (1 - \lambda_n) \right]^2.$$
 (F4)

Substituting the definition of Ec (E1b) and Cc (E2b) into Eq. (F4), it simplifies to

$$H_{CDH} = \frac{b\varepsilon^2}{g(\theta_0)} - \frac{g(\theta_0)}{2b} [Ec^2 + Cc^2]. \tag{F5}$$

By introducing Heaviside function h(x), Eqs. (F1), (F3), and (F5) can be combined into

$$H = \frac{b\varepsilon^2}{g} - \frac{g}{2b} \left[h(Ec)Ec^2 + h(Cc)Cc^2 \right], \tag{F6a}$$

$$h(x) = \begin{cases} 1, & x > 0, \\ 0, & x \le 0. \end{cases}$$
 (F6b)

REFERENCES

- ¹E. Bertrand, D. Bonn, D. Broseta, H. Dobbs, J. Indekeu, J. Meunier, K. Ragil, and N. Shahidzadeh, "Wetting of alkanes on water," J. Pet. Sci. Eng. 33, 217–222 (2002).
- ²V. Bergeron, D. Bonn, J. Y. Martin, and L. Vovelle, "Controlling droplet deposition with polymer additives," Nature **405**, 772–775 (2000).
- ³N. Shahidzadeh, E. Bertrand, J. P. Dauplait, J. C. Borgotti, P. Vié, and D. Bonn, "Effect of wetting on gravity drainage in porous media," Transp. Porous Media 52, 213–227 (2003).
- ⁴J. H. Snoeijer and B. Andreotti, "Moving contact lines: Scales, regimes, and dynamical transitions," Annu. Rev. Fluid Mech. 45, 269–292 (2013).
- ⁵X.-P. Wang, T. Qian, and P. Sheng, "Moving contact line on chemically patterned surfaces," J. Fluid Mech. **605**, 59–78 (2008).
- ⁶D. J. Durian and C. Franck, "Wetting phenomena of binary liquid mixtures on chemically altered substrates," Phys. Rev. Lett. **59**, 555 (1987).
- ⁷D. Bonn, J. Eggers, J. Indekeu, J. Meunier, and E. Rolley, "Wetting and spreading," Rev. Mod. Phys. 81, 739–805 (2009).
- ⁸Y. C. Jung and B. Bhushan, "Contact angle, adhesion and friction properties of micro-and nanopatterned polymers for superhydrophobicity," Nanotechnology 17, 4970 (2006).
- ⁹M. Iwamatsu, ^aContact angle hysteresis of cylindrical drops on chemically heterogeneous striped surfaces, J. Colloid Interface Sci. 297, 772–777 (2006).
- ¹⁰R. E. Johnson and R. H. Dettre, "Contact angle hysteresis," Adv. Chem. 43, 136-144 (1964).
- ¹¹C. Huh and S. Mason, "Effects of surface roughness on wetting (theoretical)," J. Colloid Interface Sci. **60**, 11–38 (1977).
- ¹²A. Marmur, "Contact angle hysteresis on heterogeneous smooth surfaces," J. Colloid Interface Sci. 168, 40–46 (1994).
- ¹³R. E. Johnson, Jr. and R. H. Dettre, "Contact angle hysteresis. III. Study of an idealized heterogeneous surface," J. Phys. Chem. 68, 1744–1750 (1964).
- ¹⁴S. Brandon and A. Marmur, "Simulation of contact angle hysteresis on chemically heterogeneous surfaces," J. Colloid Interface Sci. 183, 351–355 (1996).
- ¹⁵B. K. Primkulov, A. A. Pahlavan, L. Cueto-Felgueroso, and R. Juanes, "Motion of a viscous slug on heterogeneous surfaces: Crossover from stick–slip to steady sliding," J. Fluid Mech. 973, A2 (2023).
- ¹⁶J. Oliver, C. Huh, and S. Mason, "Resistance to spreading of liquids by sharp edges," J. Colloid Interface Sci. 59, 568–581 (1977).
- ¹⁷W. Li and A. Amirfazli, "A thermodynamic approach for determining the contact angle hysteresis for superhydrophobic surfaces," J. Colloid Interface Sci. 292, 195–201 (2005).
- ¹⁸S. Brandon, N. Haimovich, E. Yeger, and A. Marmur, "Partial wetting of chemically patterned surfaces: The effect of drop size," J. Colloid Interface Sci. 263, 237–243 (2003).
- ¹⁹D. Chatain, D. Lewis, J.-P. Baland, and W. C. Carter, "Numerical analysis of the shapes and energies of droplets on micropatterned substrates," Langmuir 22, 4237–4243 (2006).

- ²⁰B. Kong and X. Yang, "Dissipative particle dynamics simulation of contact angle hysteresis on a patterned solid/air composite surface," Langmuir 22, 2065-2073 (2006).
- ²¹Y. Jiang, W. Xu, M. A. Sarshar, and C.-H. Choi, "Generalized models for advancing and receding contact angles of fakir droplets on pillared and pored surfaces," J. Colloid Interface Sci. 552, 359-371 (2019).
- ²²L. W. Schwartz and S. Garoff, "Contact angle hysteresis and the shape of the three-phase line," J. Colloid Interface Sci. 106, 422-437 (1985).
- ²³Z. Zhang and X. Xu, "Effective boundary conditions for dynamic contact angle hysteresis on chemically inhomogeneous surfaces," J. Fluid Mech. 935, A34
- ²⁴N. Savva and S. Kalliadasis, "Droplet motion on inclined heterogeneous substrates," J. Fluid Mech. 725, 462-491 (2013).
- ²⁵E. Raphael and P.-G. de Gennes, "Dynamics of wetting with nonideal surfaces. The single defect problem," J. Chem. Phys. 90, 7577-7584 (1989).
- ²⁶J. Joanny and M. O. Robbins, "Motion of a contact line on a heterogeneous surface," J. Chem. Phys. 92, 3206-3212 (1990).
- ²⁷H. Kusumaatmaja and J. Yeomans, "Modeling contact angle hysteresis on chemically patterned and superhydrophobic surfaces," Langmuir 23, 6019-
- $^{\mathbf{28}}\mathrm{D.~C.}$ Pease, "The significance of the contact angle in relation to the solid surface," J. Phys. Chem. 49, 107-110 (1945).
- 29 E. Dussan, "On the spreading of liquids on solid surfaces: Static and dynamic contact lines," Annu. Rev. Fluid Mech. 11, 371-400 (1979).
- 30 J. Joanny and P.-G. De Gennes, "A model for contact angle hysteresis," J. Chem. Phys. 81, 552-562 (1984).
- ³¹M. Hatipogullari, C. Wylock, M. Pradas, S. Kalliadasis, and P. Colinet, "Contact angle hysteresis in a microchannel: Statics," Phys. Rev. Fluids 4, 044008 (2019).
- 32 L. Yan, J. C. Müller, T. L. van Noorden, B. Weigand, and A. Raoof, "Wettability-driven pore-filling instabilities: Microfluidic and numerical insights," J. Colloid Interface Sci. 696, 137884 (2025).
- 33W. D. Harkins and F. Brown, "The determination of surface tension (free surface energy), and the weight of falling drops: The surface tension of water and benzene by the capillary height method," J. Am. Chem. Soc. 41, 499-524
- 34F. Bartell and A. D. Wooley, "Solid—liquid—air contact angles and their dependence upon the surface condition of the solid," J. Am. Chem. Soc. 55, 3518-3527 (1933).
- 35 E. Schäffer and P.-z. Wong, "Contact line dynamics near the pinning threshold: A capillary rise and fall experiment," Phys. Rev. E 61, 5257 (2000).
- 36 T. Blake and Y. Shikhmurzaev, "Dynamic wetting by liquids of different viscosity," J. Colloid Interface Sci. 253, 196-202 (2002).
- ³⁷J. G. Petrov, J. Ralston, M. Schneemilch, and R. A. Hayes, "Dynamics of partial wetting and dewetting in well-defined systems," J. Phys. Chem. B 107, 1634-1645 (2003)
- ³⁸M. Vega, C. Gouttiere, D. Seveno, T. Blake, M. Voué, J. De Coninck, and A. Clarke, "Experimental investigation of the link between static and dynamic wet-
- ting by forced wetting of nylon filament," Langmuir 23, 10628–10634 (2007). ³⁹P. Nie, X. Jiang, X. Zheng, and D. Guan, "Manipulation of contact angle hysteresis at electrified ionic liquid-solid interfaces," Phys. Rev. Lett. 132, 044002
- ⁴⁰C. Timmons and W. Zisman, "The effect of liquid structure on contact angle hysteresis," J. Colloid Interface Sci. 22, 165-171 (1966).

- ⁴¹F. J. Holly and M. F. Refojo, "Wettability of hydrogels I. Poly (2-hydroxyethyl methacrylate)," J. Biomed. Mater. Res. 9, 315-326 (1975).
- ⁴²H. Yasuda, A. K. Sharma, and T. Yasuda, "Effect of orientation and mobility of polymer molecules at surfaces on contact angle and its hysteresis," J. Polym. ci. Polym. Phys. Ed. 19, 1285-1291 (1981).
- ⁴³C. N. Lam, R. Wu, D. Li, M. Hair, and A. Neumann, "Study of the advancing and receding contact angles: Liquid sorption as a cause of contact angle hysteresis," Adv. Colloid Interface Sci. 96, 169-191 (2002).
- 44 M. Pradas, N. Savva, J. B. Benziger, I. Kevrekidis, and S. Kalliadasis, "Dynamics of fattening and thinning 2D sessile droplets," Langmuir 32, 4736-4745 (2016).
- 45W. S. Wong, L. Hauer, A. Naga, A. Kaltbeitzel, P. Baumli, R. Berger, M. D'Acunzi, D. Vollmer, and H.-J. Butt, "Adaptive wetting of polydimethylsiloxane," Langmuir 36, 7236-7245 (2020).
- ⁴⁶X. Li, S. Silge, A. Saal, G. Kircher, K. Koynov, R. Berger, and H.-J. Butt, "Adaptation of a styrene-acrylic acid copolymer surface to water," Langmuir **37**, 1571–1577 (2021).
- ⁴⁷X. Chang, H. Huang, X.-Y. Lu, and J. Hou, "Width effect on contact angle hysteresis in a patterned heterogeneous microchannel," J. Fluid Mech. 949, A15 (2022).
- ⁴⁸X. Xu and X. Wang, "Analysis of wetting and contact angle hysteresis on chemically patterned surfaces," SIAM J. Appl. Math. 71, 1753-1779 (2011).
- ⁴⁹J. Zhang, F. Müller-Plathe, and F. Leroy, "Pinning of the contact line during evaporation on heterogeneous surfaces: Slowdown or temporary immobilization? insights from a nanoscale study," Langmuir 31, 7544-7552 (2015).
- 50X. Shan and H. Chen, "Lattice Boltzmann model for simulating flows with multiple phases and components," Phys. Rev. E 47, 1815 (1993).
- ⁵¹C. Luo and T. Tagawa, "Enhanced boiling heat transfer on structured surfaces with linear and staggered arrangements of hydrophilic and hydrophobic micropillars," Int. J. Heat Mass Transfer 225, 125394 (2024). ⁵²Z.-W. He, C. Shu, and Z. Chen, "Simplified lattice Boltzmann method on
- multi-resolution mesh," Phys. Fluids 36, 087171 (2024).
- 53X. Shan and G. Doolen, "Multicomponent lattice-Boltzmann model with interparticle interaction," J. Stat. Phys. 81, 379-393 (1995).
- ⁵⁴P. Yuan and L. Schaefer, "Equations of state in a lattice Boltzmann model," Phys. Fluids 18, 042101 (2006).
- 55H. Huang, M. Sukop, and X. Lu, Multiphase Lattice Boltzmann methods: Theory and Application (John Wiley & Sons, 2015).
- 56Z.-H. Chai and T.-S. Zhao, "A pseudopotential-based multiple-relaxation-time lattice Boltzmann model for multicomponent/multiphase flows," Acta Mech. Sin. 28, 983-992 (2012).
- ${\bf ^{57}}{\rm D.}$ Hessling, Q. Xie, and J. Harting, "Diffusion dominated evaporation in multicomponent lattice Boltzmann simulations," J. Chem. Phys. 146, 054111 (2017).
- 58D. P. Ziegler, "Boundary conditions for lattice Boltzmann simulations," J. Stat. Phys. 71, 1171-1177 (1993).
- 59C. Priest, R. Sedev, and J. Ralston, "A quantitative experimental study of wetting hysteresis on discrete and continuous chemical heterogeneities," Colloid Polym. Sci. 291, 271-277 (2013).
- 60Y. J. Wang, S. Guo, H.-Y. Chen, and P. Tong, "Understanding contact angle hysteresis on an ambient solid surface," Phys. Rev. E 93, 052802 (2016).
- ⁶¹A. Fakhari and D. Bolster, "Diffuse interface modeling of three-phase contact line dynamics on curved boundaries: A lattice Boltzmann model for large density and viscosity ratios," J. Comput. Phys. 334, 620-638 (2017).